



## RESEARCH ARTICLE

# UV-induced degradation of high-efficiency silicon PV modules with different cell architectures

Archana Sinha<sup>1</sup>  | Jiadong Qian<sup>2</sup> | Stephanie L. Moffitt<sup>1</sup> | Katherine Hurst<sup>2</sup> | Kent Terwilliger<sup>2</sup> | David C. Miller<sup>2</sup>  | Laura T. Schelhas<sup>2</sup>  | Peter Hacke<sup>2</sup> 

<sup>1</sup>SLAC National Accelerator Laboratory, Menlo Park, California, USA

<sup>2</sup>National Renewable Energy Laboratory, Golden, Colorado, USA

## Correspondence

Laura Schelhas and Peter Hacke, National Renewable Energy Laboratory, Golden, CO 80401, USA.

Email: [laura.schelhas@nrel.gov](mailto:laura.schelhas@nrel.gov) and [peter.hacke@nrel.gov](mailto:peter.hacke@nrel.gov)

## Funding information

U.S. Department of Energy (DOE), Office of Energy Efficiency and Renewable Energy, Solar Energy Technologies Office, Grant/Award Number: 32509; U.S. Department of Energy (Office of Science, Office of Basic Energy Sciences and Energy Efficiency and Renewable Energy, Solar Energy Technology Program), Grant/Award Number: DE-AC36-08GO28308; National Science Foundation, Grant/Award Number: ECCS-2026822

## Abstract

Degradation from ultraviolet (UV) radiation has become prevalent in the front of solar cells due to the introduction of UV-transmitting encapsulants in photovoltaic (PV) module construction. Here, we examine UV-induced degradation (UVID) in various commercial, unencapsulated crystalline silicon cell technologies, including bifacial silicon heterojunction (HJ), interdigitated back contact (IBC), passivated emitter and rear contact (PERC), and passivated emitter rear totally diffused (PERT) solar cells. We performed UV exposure tests using UVA-340 fluorescent lamps at  $1.24 \text{ W}\cdot\text{m}^{-2}$  (at 340 nm) and  $45^\circ\text{C}$  through  $4.02 \text{ MJ}\cdot\text{m}^{-2}$  (2000 h). Our results showed that modern cell architectures are more vulnerable to UVID, leading to a significant power decrease ( $-3.6\%$  on average;  $-11.8\%$  maximum) compared with the conventional aluminum back surface field (Al-BSF) cells ( $<-1\%$  on average). The power degradation is largely caused by the decrease in short-circuit current and open-circuit voltage. A greater power decrease is observed in bifacial cells with rear-side exposure compared with those with front-side exposure, indicating that the rear side is more susceptible to UV damage. Secondary ion mass spectroscopy (SIMS) confirmed an increase in hydrogen concentration near the Si/passivation interface in HJ and IBC cells after UV exposure; the excess of hydrogen could result in hydrogen-induced degradation and subsequently cause higher recombination losses. Additionally, surface oxidation and hot-carrier damage were identified in PERT cells. Using a spectral-based analysis, we obtained an acceleration factor of  $5\times$  between unpackaged cells (containing a silicon nitride antireflective coating on the front) in the UV test and an encapsulated module (with the front glass and encapsulant blocking 90% of the UV at 294 nm and 353 nm, respectively) in outdoor conditions. From the analytical calculations, we show that a UV-blocking encapsulant can reduce UV transmission in the module by an additional factor of  $\sim 50$ .

## KEYWORDS

bifacial, crystalline silicon, recombination, surface passivation, UV-induced degradation

This is an open access article under the terms of the [Creative Commons Attribution](https://creativecommons.org/licenses/by/4.0/) License, which permits use, distribution and reproduction in any medium, provided the original work is properly cited.

© 2022 The Authors. Progress in Photovoltaics: Research and Applications published by John Wiley & Sons Ltd.

## 1 | INTRODUCTION

After years of improvement in photovoltaic (PV) module performance, including the reduction of power degradation rates toward a mean of  $-0.5\% \cdot \text{year}^{-1}$  to  $-0.6\% \cdot \text{year}^{-1}$  for crystalline silicon (c-Si) technology,<sup>1</sup> there are new pieces of evidence that the degradation rates for many c-Si modules are now increasing. For example, Trina Solar published an approximate  $-4.5\% \cdot \text{year}^{-1}$  degradation rate for multiple module types mounted in Singapore, and the Department of Energy (DOE) National Laboratory Regional Test Center program showed degradation of  $-1\% \cdot \text{year}^{-1}$  to  $-2\% \cdot \text{year}^{-1}$  for various types of high-efficiency c-Si modules, even after initial light-induced degradation (LID) stabilization.<sup>2</sup> The increased initial PV performance of next-generation high-efficiency solar cells has been attributed to the high-quality wafers and their longer carrier lifetimes. Improvements in carrier lifetimes are due in part to improved surface passivation. However, the recent increase in power degradation rates of modern cell types is concerning and needs to be better understood and addressed if c-Si modules are to reach a 50-y module lifetime.

Historically, the harmful effects of UV radiation have largely been associated with the aging of module packaging materials and have led to encapsulant discoloration,<sup>3,4</sup> delamination,<sup>5,6</sup> and backsheet cracking.<sup>7,8</sup> Solar cell performance is also adversely affected by UV radiation through the generation of surface defects.<sup>9–12</sup> To avoid carrier recombination at defects and improve minority carrier lifetimes, the cell surfaces are generally passivated using dielectric layers, such as hydrogenated silicon nitride ( $\text{Si}_x\text{N}_y\text{:H}$ ) and/or silicon dioxide ( $\text{SiO}_2$ ). However, UV exposure can disrupt this surface passivation by damaging the passivation layer itself or the passivation layer/Si cell interface<sup>11–14</sup> as well as causing subsurface damage in the silicon.<sup>15,16</sup> Different research groups have identified distinct wavelengths in the 300–400 nm spectral range as the damaging wavelengths of incident radiation for UV degradation of Si solar cells.<sup>13,14,17–24</sup>

Emerging higher performance cell technologies, such as p-type passivated emitter and rear contact (p-PERC) and n-type passivated emitter rear totally diffused (n-PERT) cells, have been observed to be more sensitive to UV radiation.<sup>21</sup> Additionally, as bifacial modules gain market share, it is important to consider that both the front and back of the bifacial cell are potentially susceptible to UV-induced degradation (UVID).<sup>20</sup> UVID can be characterized by a gradual loss in module performance. For example, JinkoSolar published an efficiency loss of  $-4\%$  to  $-7\%$  in industrial solar cells after exposure to approximately  $540 \text{ MJ} \cdot \text{m}^{-2}$  ( $150 \text{ kWh} \cdot \text{m}^{-2}$ , i.e., 25 sunny days AM1.5G) of UVA light.<sup>25</sup> In some PERT cells, a UV dose of  $1.8 \text{ GJ} \cdot \text{m}^{-2}$  at  $40^\circ\text{C}$  resulted in 15% power loss.<sup>21</sup> We note that the UVID described here results from the surface region and/or interface effect(s)—distinct from the typical LID (a fast initial power decrease attributed to the evolution of boron-oxygen and boron-iron complexes in the bulk of silicon)<sup>26,27</sup> and light and elevated temperature induced degradation (“LETID,” a slow progressing degradation activated during light exposure or via electrical current at temperatures above  $60^\circ\text{C}$ ).<sup>28,29</sup>

In silicon solar cells, significant cell degradation has been observed under UV exposure, which is generally done with either

concentrated sunlight or xenon arc lamps.<sup>11–14</sup> Gruenbaum et al. reported an increase in recombination centers at the Si/SiO<sub>2</sub> interface due to UV light photoinjecting electrons from the silicon conduction band into silicon dioxide. UV exposure is effective in disrupting surface passivation by changing the fixed charge density and increasing the interface defect density near the Si surface.<sup>30,31</sup> One explanation for the vulnerability of  $\text{Si}_x\text{N}_y$  passivation arises from the deposition processes of  $\text{Si}_x\text{N}_y$  films. Transmission electron microscopy (TEM) examination revealed that during plasma-enhanced chemical vapor deposition (PECVD), a damaged layer of around 50 nm is formed at the c-Si side of  $\text{Si}_x\text{N}_y$ /Si interface, which is passivated with H atoms.<sup>15</sup> However, the recombination velocity at this region is increased by the UV irradiation, resulting in a decrease in carrier lifetime. Another paper revealed that subsequent etching and removal of the damaged passivation and defect layer tend to recover the carrier lifetime.<sup>16</sup> Further, the defects in the damaged layer were electrically inactivated due to high-temperature annealing ( $600^\circ\text{C}$ ) and thereby resulting increase in the effective lifetime.<sup>32</sup>

The generation of hot carriers (either electrons or holes) is another proposed UV damage mechanism.<sup>12</sup> For example, hot electrons can be generated when a high-energy photon (i.e., UV radiation) excites an electron out of the valence band and beyond the conduction band. Hot carriers are extremely mobile and have sufficient energy to surpass an interfacial potential barrier, allowing them to be injected across the interface when the carrier concentration exceeds  $1.5 \times 10^{17} \text{ cm}^{-3}$ .<sup>10</sup> The hot carriers generated in Si cells can have sufficient kinetic energy to damage the passivation layer and increase the interface state density. Hot carriers are more prevalent in PV devices that operate under the extraterrestrial solar spectrum, concentrated sunlight, or high electrical current. There are many reports in the literature concerning the effects of oxidation and other processing variables on hot-electron damage.<sup>33</sup> For instance, texturization, trichloroethane oxidation, and an aluminum anneal all contribute to the instability of the passivation interfaces. Dry thermal oxides (hot-carrier resistant) or poly-Si (block water) can provide good protection from hot carrier damage.<sup>34</sup> Once damaged, it may be possible to anneal at  $250\text{--}300^\circ\text{C}$  to restore the correct charge state. There is evidence that at least some of the generated interface defects are hydrogen-related. Gruenbaum et al.<sup>9</sup> found that the defects could be recovered fully by annealing in a hydrogen-containing atmosphere but only partially in nitrogen. Buchanan et al.<sup>35</sup> correlated the electron injection and generation of interface traps with the release of trapped hydrogen in the oxide and its migration to the interface. They inferred a threshold electron energy of  $\sim 2 \text{ eV}$  in excess of the oxide conduction band for both the hydrogen release and defect generation.

Previous studies suggest several possible degradation mechanisms associated with UV exposure, but the UV stability of modern cell types is not well understood. The current manuscript focuses on identifying the UV susceptibility of a variety of contemporary PV cells, distinguishing between their photovoltaic performance, composition, and optical performance through UV aging. We sought to identify the most affected types of cells and differentiate the degradation

mechanisms enabling UVID. Understanding the damaging effects of UV radiation in emerging silicon solar cell technologies will enable the identification of the underlying mechanisms that may affect both the power output and durability of modules.

## 2 | APPROACH

### 2.1 | Test samples

We carried out the experiment on a variety of unencapsulated, commercial c-Si solar cell architectures, as outlined in Table 1. The test samples are grouped by cell technology; different cell makes are designated with a letter index (A–L). The sample set includes high-efficiency silicon cell technologies, such as heterojunction (HJ), interdigitated back contact (IBC), PERT, and PERC cells. We compared the performance of these cells against the conventional legacy aluminum back surface field (Al-BSF) cells. The samples used in this study were cut from high-efficiency cells (in the order of 20%, or around 15% for

the legacy Al-BSF). Detailed descriptions of cell dicing and tabbing interconnection are described in Section S1 of the Supporting Information. Both mono- and multi-crystalline cells were examined. **The set also includes bifacial cells, which were irradiated from both the front and rear sides to study the UV sensitivity of each face.** In the case of bifacial IBC cells, the rear side features an open metallization grid where UV light is transmitted/absorbed in the narrow gap between p and n connected fingers. At least three replicas of each cell type were chosen to increase the confidence in the average results and to identify outlying measurements.

The test samples were mounted on in-house designed fixtures at NREL, made of polyoxymethylene for protection and handling of the cells throughout UV testing. The test fixture featured a black mask to avoid optical reflection to the cell from the surrounding white surfaces, as shown in Figure 1A. SLAC used the chamber manufacturer's standard specimen holders, which are made of clear anodized aluminum, as displayed in Figure 1B. The base surface of the holder was masked with polyimide tape to provide electrical insulation to the cells.

**TABLE 1** Details of cell technologies considered for identical UV screen tests, depending on the sample type, at the National Renewable Energy Laboratory (NREL) and SLAC National Accelerator Laboratory (SLAC)

Cell technology	Index	Crystalline type	Bifacial	Front structure	Rear structure	Cells tested
HJ	A <sup>a,b</sup>	Mono	Y	ITO/(p <sup>+</sup> )a-Si/(i)a-Si	n Si/(i)a-Si/(n <sup>+</sup> )a-Si/ITO	6
IBC	B <sup>a</sup>	Mono	Y	Si <sub>x</sub> N <sub>y</sub> /SiO <sub>2</sub> /(n <sup>+</sup> )Si	-	3
	C <sup>a,b</sup>	Mono	Y	Si <sub>x</sub> N <sub>y</sub> /SiO <sub>2</sub> /(p <sup>+</sup> )Si/n Si	n Si/Si <sub>x</sub> N <sub>y</sub>	6
	D <sup>a</sup>	Mono	N	Si <sub>x</sub> N <sub>y</sub> /SiO <sub>2</sub> /(p <sup>+</sup> )Si/n Si	-	3
n-PERT	E <sup>a,b</sup>	Mono	Y	Si <sub>x</sub> N <sub>y</sub> /SiO <sub>2</sub> /(p <sup>+</sup> )Si/n Si	n Si/Si <sub>x</sub> N <sub>y</sub>	6
	F <sup>b</sup>	Mono	N	Si <sub>x</sub> N <sub>y</sub> /SiO <sub>2</sub> /(p <sup>+</sup> )Si/n Si	-	3
p-PERC	G <sup>a,b</sup>	Mono	Y	Si <sub>x</sub> N <sub>y</sub> /SiO <sub>x</sub> /(n <sup>+</sup> )Si/p Si	p Si/AlO <sub>x</sub> /Si <sub>x</sub> N <sub>y</sub>	6
	H <sup>a,b</sup>	Mono	N	Si <sub>x</sub> N <sub>y</sub> /(n <sup>+</sup> )Si/p Si	p Si/Si <sub>x</sub> N <sub>y</sub>	3
	I <sup>a</sup>	Mono	N	Si <sub>x</sub> N <sub>y</sub> /(n <sup>+</sup> )Si/p Si	-	3
	J <sup>a</sup>	Mono	Y	Si <sub>x</sub> N <sub>y</sub> /SiO <sub>x</sub> /(n <sup>+</sup> )Si/p Si	p Si/AlO <sub>x</sub> /Si <sub>x</sub> N <sub>y</sub>	3
	K <sup>a</sup>	Multi	Y	Si <sub>x</sub> N <sub>y</sub> /SiO <sub>x</sub> /(n <sup>+</sup> )Si/p Si	p Si/AlO <sub>x</sub> /Si <sub>x</sub> N <sub>y</sub>	3
Al-BSF	L <sup>a,b</sup>	Multi	N	Si <sub>x</sub> N <sub>y</sub> /(n <sup>+</sup> )Si/p Si	-	6

<sup>a</sup>National Renewable Energy Laboratory (NREL).

<sup>b</sup>SLAC National Accelerator Laboratory (SLAC).

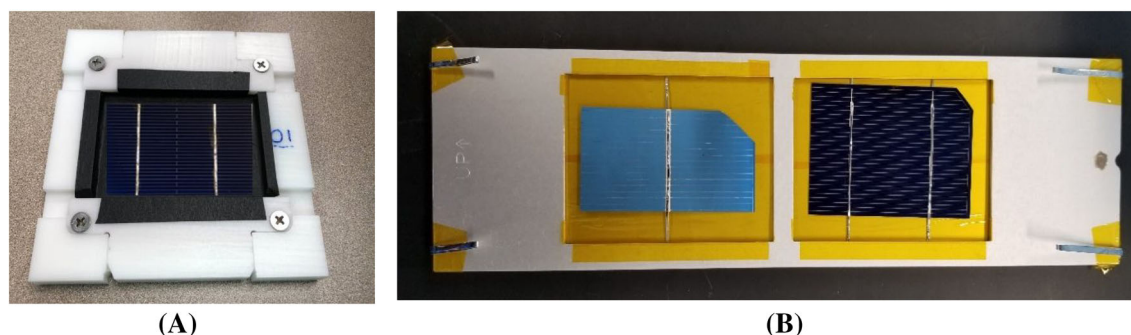


**FIGURE 1** Carrier fixtures used at (A) NREL and (B) SLAC chambers, both featuring special masking to reduce the optical reflection and provide electrical insulation to the unencapsulated solar cells

## 2.2 | Outdoor preconditioning

Prior to UV exposure tests in the weathering chambers, the test samples were preconditioned in natural sunlight for a cumulative broad-band dose of  $\geq 15$  kWh to stabilize against boron-oxygen (B-O) LID. The cells were placed under a museum-grade acrylic glass sheet (UF-5, Arkema S.A.; 100% light blocking below 404 nm) to filter the UV radiation. The cell temperature was also periodically monitored using a calibrated thermocouple to ensure it stayed below 45°C, averting the activation of LETID.

## 2.3 | Accelerated UV exposure test

We carried out identical UV exposure testing at two national labs, NREL and SLAC, to evaluate the magnitude of cell degradation and to compare the degradation of cells under different electrical load configurations (i.e., open-circuit condition versus short-circuit condition). The front and rear sides of bifacial cells were also selectively irradiated. At NREL, we carried out these tests in a custom UV chamber, and at SLAC, we used a QUV chamber (QUV, Q-Lab Corporation) equipped with built-in feedback control for irradiance and temperature calibration. Both chambers were equipped with Q-Lab UVA-340 lamps that simulate the sun's spectrum at the critical short-wavelength region from 365 nm down to the solar cutoff of 295 nm, with peak emission at 340 nm. For this study, the bare cells were directly exposed to the UVA-340 fluorescent lamps at an illumination intensity of  $1.24 \text{ W} \cdot \text{m}^{-2} \cdot \text{nm}^{-1}$  at 340 nm ( $\sim 2.5 \times$  UV suns), chamber air temperature of  $45 \pm 2^\circ\text{C}$ , and uncontrolled operating humidity of  $\sim 7\%$ , resulting in a cell chamber temperature ( $45 \pm 2^\circ\text{C}$ ). The cell temperature was kept low to prevent inadvertent activation of LETID.<sup>8</sup> Most of the cells were UV stressed under open-circuit configuration (i.e., no load connection), although selected cells were also short-circuited to enhance the hot-electron damage. The test duration in this study was 2000 h, which is equivalent to approximately 2 years of outdoor incident UV irradiation in Phoenix, Arizona, USA.<sup>36</sup> Assuming an ideal sunny day at solar noon, as in Habte et al.,<sup>37</sup> we converted the chamber UV dose at 340 nm (equivalent to  $4.02 \text{ MJ} \cdot \text{m}^{-2}$ ) to the measured outdoor cumulative exposure from the measured wavelength range of 295–385 nm (averaged from years 2000–2020) using the Simple Model of the Atmospheric Radiative Transfer of Sunshine (SMARTS) code.<sup>38,39</sup> Because the controlled chamber dose was converted relative to the measured outdoor dose, the daylight hours and weather history (cloudiness) were also considered.

## 2.4 | Characterization

To investigate degradation in cells after UV exposure, we employed several characterization methods, including current-voltage (*I*-*V*) testing, spectral reflectance measurements, secondary ion mass spectroscopy (SIMS), and X-ray photoelectron spectroscopy (XPS). *I*-*V* and

spectral reflectance measurements were used to examine the changes in the electrical and optical performance of the cell, respectively. SIMS was primarily used to measure the hydrogen distribution at the interface and bulk of Si, whereas XPS was used to examine the surface chemistry. Detailed descriptions of these characterization methods are provided in Section S2.

## 2.5 | Spectral optical modeling of UVID

To better quantify the UV dose for the unpackaged cells used in this study relative to a PV module, as well as to help diagnose the degradation mechanism for UVID, we developed an optical model for c-Si modules containing  $\text{Si}_x\text{N}_y$  antireflective coating on the front side (excluding HJ cells). While the analysis and verification of the optical effect of the indium tin oxide (ITO) layer of HJ cells are outside the scope of this work, the measured reflectance of the cell surfaces may be used as a first estimate to compare the UV irradiance at the  $\text{Si}_x\text{N}_y/\text{Si}$  interfaces on the cell surfaces (Figure S1). Because the optical performance of antireflective coatings may vary significantly with UV wavelength and also between makes of cells, future study is recommended. The spectral absorptance of each module layer and the spectral reflectance of each interface were evaluated so that a transfer function could be determined for the incident optical flux at the  $\text{Si}_x\text{N}_y$  layer and c-Si cell surfaces. All spectra were evaluated in 1-nm increments, from at least 250 nm to 2500 nm. Thin-film layers that were considered include the antireflective coating on the front glass,  $\text{AR}_g$ , and the antireflective coating on the cell surface,  $\text{AR}_c$ . The optical performance was evaluated using the approach in Miller.<sup>40</sup> Briefly, the transmittance ( $\tau_i$ , dimensionless) and reflectance ( $\rho_i$ , dimensionless) of individual components (e.g., glass) were measured so that the complex refractive index could be iteratively evaluated to a converged solution. The optical performance of coupons (e.g.,  $\text{AR}_g/\text{glass}$ ,  $\text{glass}/\text{encapsulant}/\text{glass}$ , and  $\text{glass}/\text{encapsulant}/\text{cell}$ ) was measured to assess material stacks or bulk materials (encapsulant). Bulk/thin-film/bulk material stacks (e.g.,  $\text{air}/\text{AR}_g/\text{glass}$  and  $\text{encapsulant}/\text{AR}_c/\text{Si}$ ) were compared with an analytic model.<sup>41</sup> The complex refractive index of a representative  $\text{Si}_x\text{N}_y$   $\text{AR}_c$  thin film was determined using ellipsometry. All samples were examined in an unaged condition. The complex refractive index of  $\text{Si}$ <sup>42,43</sup> and the terrestrial, real refractive index of  $\text{air}$ <sup>42</sup> were taken from the literature. The source spectra for the NREL custom chamber used in this study were verified using an OL 756 spectrometer with an OL IS-670 integrating sphere (Optronic Laboratories, LLC). Once the refractive index was known, the absorptance was determined from the Beer-Lambert law, and the reflectance was determined from Snell's law. The transfer function ( $F_t$ ) for the cell or module was then determined from the product of the reflectance ( $\rho$ ) and absorptance ( $\alpha$ ) events occurring along the optical path (see Equation 1).

$$F_t[\lambda] = \prod_{i=1}^n \left(1 - \frac{\rho_{2i}}{100}\right) \left(1 - \frac{\alpha_{2i+1}}{100}\right) \quad (1)$$

### 3 | RESULTS AND DISCUSSION

In this section, we first compare the UV susceptibility of different modern unencapsulated cell types in a UV screening experiment. Section 3.2 presents the results from multiple characterization techniques, including *I*-*V*, SIMS, XPS, and optical reflectance. The extensive chemical and optical characterizations were employed on select cell makes to diagnose the degradation mechanism(s) for the cells showing the greatest power degradation from UV exposure. Because only a subset of the samples was examined in detail, the diagnosis may not apply universally within a given cell technology, and the variation between makes of cells cannot be assessed. Section 3.3 describes the test results of cells under open-circuit and short-circuit conditions and the associated hot-electron damage in the cells.

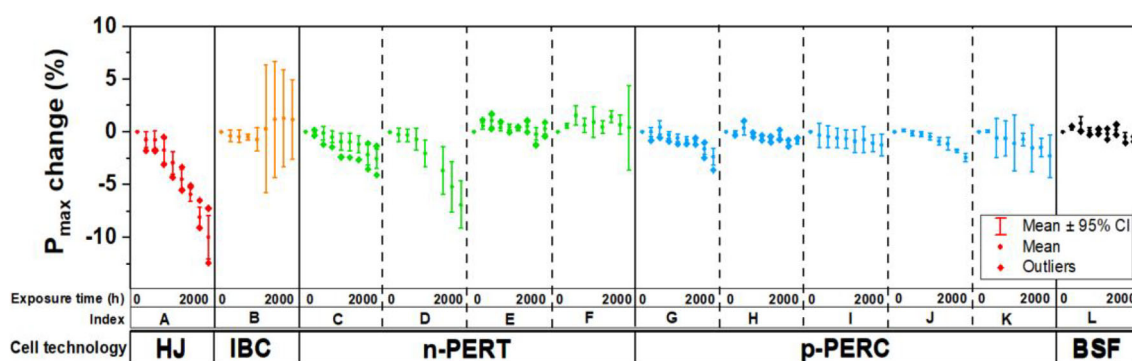
#### 3.1 | UVID in unencapsulated cells

Figure 2 shows the percent change in maximum power ( $P_{max}$ ) of unencapsulated cells with front surfaces irradiated over a 2000-h UV exposure test at NREL and SLAC. The statistical confidence in measured  $P_{max}$  is shown here, while that of other *I*-*V* parameters is shown in Figure S2. The greatest  $P_{max}$  degradation was observed in the HJ cells, followed by the n-PERT and p-PERC cells, whereas the power decrease was least pronounced in their Al-BSF counterparts. The time evolution of  $P_{max}$  degradation in most of the cell types follows a linear trend, except for “A<sub>HJ</sub>” and “D<sub>PERT</sub>,” which show a non-linear or exponential decrease. We determined the  $P_{max}$  degradation rate by assuming an initial linear power reduction, as in Figure 2 (also reported in several studies<sup>44,45</sup>). We find that HJ cells suffer from the greatest power loss, of  $-5.46\%\text{-year}^{-1}$  (average), with a maximum degradation rate of  $-8\%\text{-year}^{-1}$ . The  $P_{max}$  of p-PERC and n-PERT cells degrades at an average rate of  $-1\%\text{-year}^{-1}$ , whereas the  $P_{max}$  of Al-BSF cells degrades at  $-0.36\%\text{-year}^{-1}$ . IBC cells showed a different behavior: the cells exhibited a slight increase in power. Note that the rapid power loss observed in our UV stress

testing was obtained on the bare (unpackaged) cells. The equivalent power loss in a packaged module was determined using a spectral analysis, which is presented in Section 3.4. Further, the degradation trajectory varies for different cell types within the same PV technology, indicating that the degradation mechanism is influenced by more than just cell technology, and depends on the materials and manufacturing processes used.

Figure 3 shows the final degradation after 2000 h of UV exposure in every cell type, including the bifacial cells (indexed as +). Most of the bifacial cells with rear-side exposure exhibited a greater  $P_{max}$  decrease than those with front-side exposure, indicating that the rear side of the bifacial cell is more vulnerable to UV radiation. This could result from differences in the surface field and passivation schemes used on the front versus rear sides, making the rear side more susceptible to UV degradation. The average  $P_{max}$  degradation rate observed on the rear side of bifacial cells is  $-2.4\%\text{-year}^{-1}$ , in contrast to  $-1.4\%\text{-year}^{-1}$  on the front side. Note that the total UV dose on each side of the bifacial cells under testing was the same; however, during actual field operation, the back surfaces of bifacial modules receive only a fraction of UV radiation compared to the front surfaces, depending on the mounting position, ground albedo, and presence of UV absorbers in the module packaging materials. Although not specifically examined here, the number and thickness of the layers may vary between the front and back of the cells, readily affecting the UV dose within the AR<sub>c</sub> and its interface with the cell.

To see the variability of UVID on each cell type and its correlation with the governing characteristic power loss, we studied the cell electrical parameters separately. Figure 3 shows the percent change in each *I*-*V* parameter after 2000 h of UV irradiation. We found that the contributing factors to  $P_{max}$  degradation are not the same for all cell technologies. The  $P_{max}$  degradation in HJ cells is driven by significant decreases in fill factor (*FF*) and open-circuit voltage ( $V_{oc}$ ), whereas in the PERT cell technology, degradation primarily results from short-circuit current ( $I_{sc}$ ) and  $V_{oc}$  losses, as shown in Figure 4. IBC cells exhibited a slight increase in power, despite a decrease in both  $I_{sc}$  and  $V_{oc}$ .



**FIGURE 2** Change in  $P_{max}$  for all replicates of each cell type along with a 95% confidence interval in the measurement at each read point, up to 2000 h of UV irradiation under front-side exposure. A negative value indicates degradation. Most of the cell types underwent linear power degradation



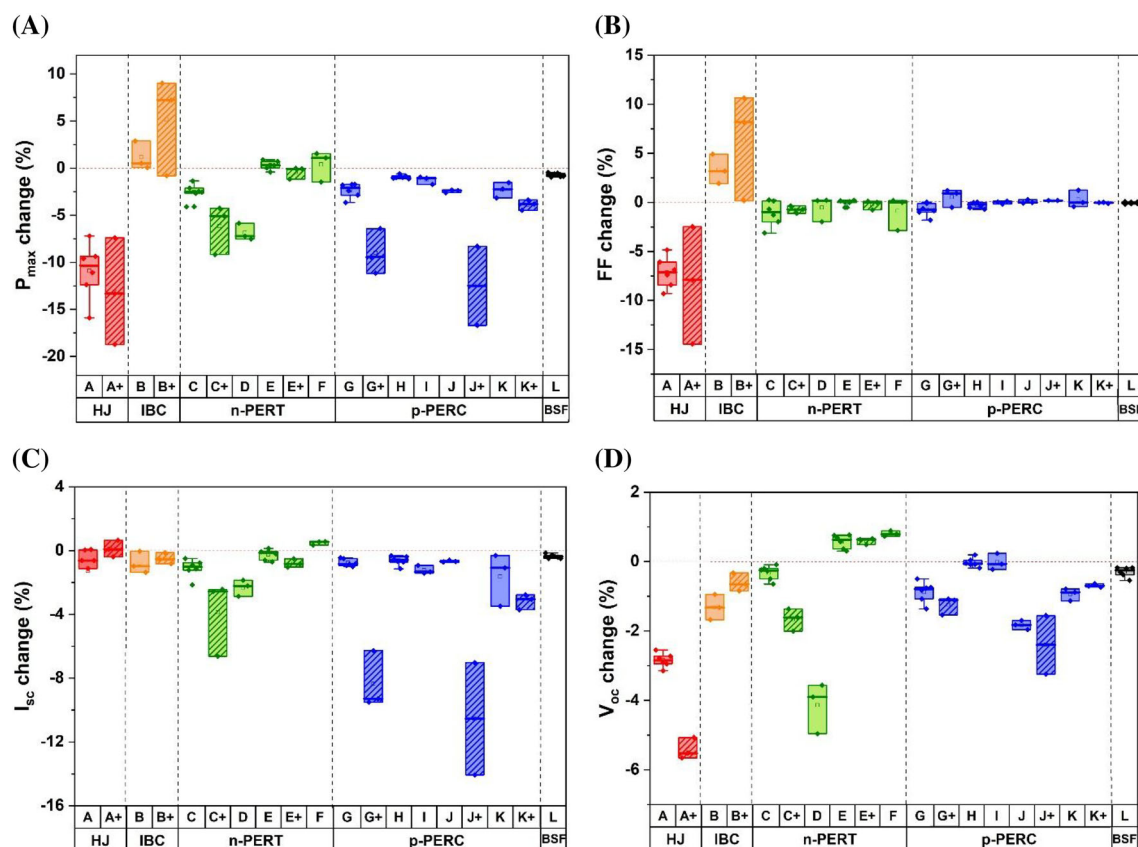


**FIGURE 3** Final change in I–V parameters of test cells after 2000 h of UV exposure testing, partitioned by cell technology and cell type. The data corresponding to rear-side exposure of bifacial cells is indexed as +. The same side of the cell was illuminated during the I–V measurements as it was facing the UV lamps in the screen test. This shows the UV sensitivity of the front and rear sides of the bifacial cell. As a guide to the eye, a 0% change is indicated by a red dotted line. The 25%–75% confidence intervals are denoted by boxes, and the mean and median are indicated by a square and crossbar, respectively

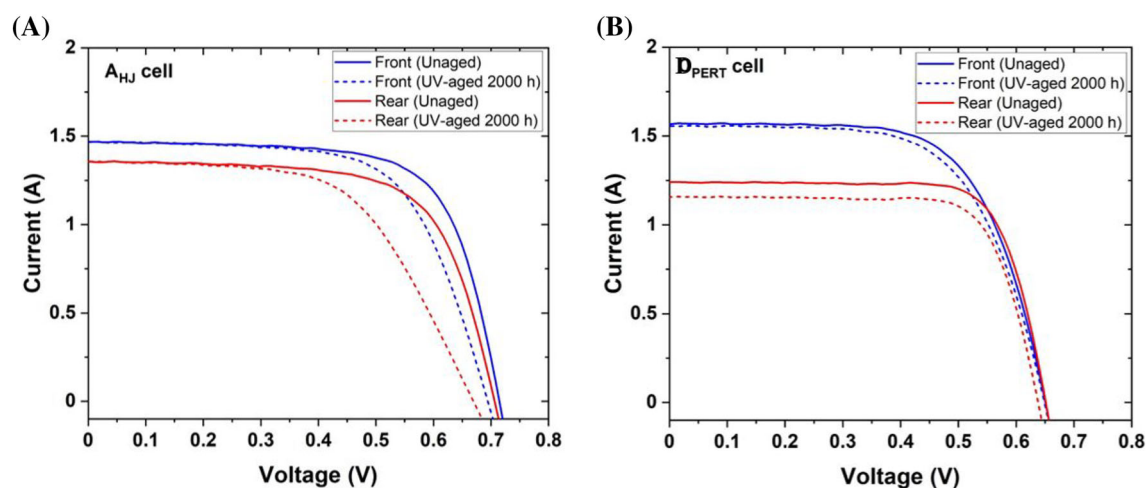


**FIGURE 4** I–V curves for bifacial (A)  $A_{HJ}$  and (B)  $D_{PERT}$  cells, obtained with front-side illumination (blue) and rear-side illumination (red), before (solid) and after (dashed) 2000 h of UV exposure testing on the same side

## 3.2 | UVID and Si/passivation damage

### 3.2.1 | HJ cells

Figure 3 shows that the average rapid power loss observed in HJ cells after UV exposure on the front side is  $-11\%$ . This power loss is dominated by a decline in  $V_{oc}$  ( $-3\%$ ) and  $FF$  ( $-7\%$ ) while the  $I_{sc}$  decrease ( $-1\%$ ) contributes the least. Similarly, the average degradation observed on the rear side of HJ cells in  $P_{max}$ ,  $V_{oc}$ ,  $FF$ , and  $I_{sc}$  is  $-14\%$ ,  $-6\%$ ,  $-3.5\%$ , and  $-1\%$ , respectively. A significant increase in series resistance ( $R_s$ ) is observed from the  $I$ - $V$  curve slope at  $V_{oc}$  (shown in Figure 4A), which could be attributed to an increase in sheet resistance of the ITO front electrode or deterioration of the ITO/a-Si and (p)a-Si/(i)a-Si passivating interfaces. No obvious signs of delamination, corrosion, intermetallic reaction, or grain growth were observed for the gridlines in optical microscopy (Figure S3). The comparison of dark  $I$ - $V$  curves before and after UV exposure indicated an increase in  $R_s$  as well as in the diode ideality factor and recombination current (Figure S4). Similarly, Jordan et al. reported the non-linear power loss in 10-year-old fielded HJ modules, where most degradation occurred

in the first 2 years and was attributed to significant  $V_{oc}$  losses and a small decrease in  $FF$ . The  $V_{oc}$  decrease was ascribed to an increase in carrier recombination, whereas  $FF$  degradation is primarily caused by an increase in  $R_s$ .<sup>46</sup> It is important to note that the HJ cell examined was the most affected of the specific manufacturer in this study; therefore, the observed power degradation may not apply to all cells independent of cell structure.

UVID was previously associated with hydrogen redistribution across the passivation layer and the silicon bulk in the cell.<sup>47</sup> To quantify H distribution as a result of UV exposure, we used SIMS, as this technique offers good sensitivity in detecting H and other trace elements. Figure 5A displays the SIMS depth profiles of Si, O, and H elements acquired on the ITO-etched surface of the  $A_{HJ}$  sample. The depth scale was chosen so that the etched surface would correspond to the ITO/(p)a-Si interface. It should be noted that only the H concentration is quantified and presented in  $\text{atoms}\cdot\text{cm}^{-3}$  (right y-axis), whereas the intensities of other elements are presented in arbitrary units (left y-axis). There are two inflections in the H profile (red), which correspond to the a-Si and c-Si regions, respectively. The H profile of the UV-aged sample shows higher H concentration across

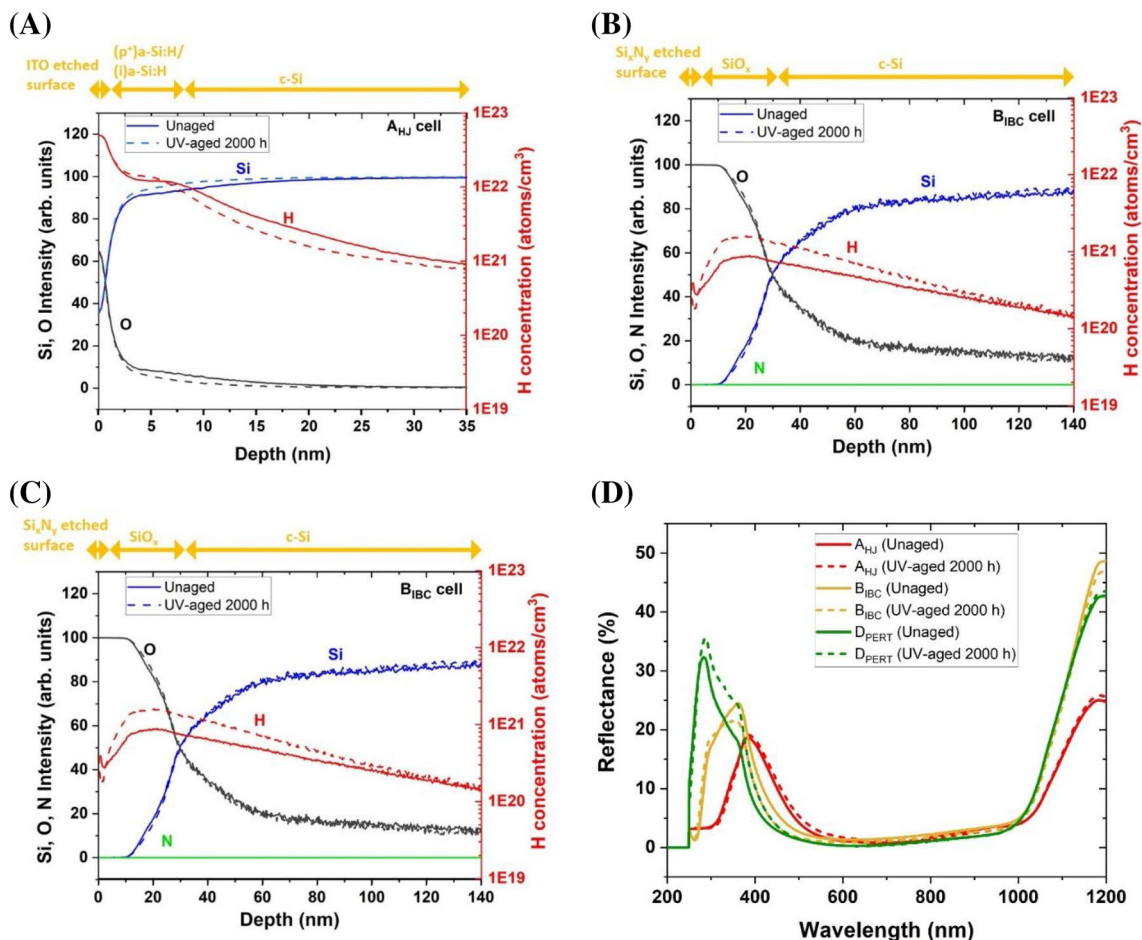


**FIGURE 5** (A–C) SIMS depth profiles of unaged and 2000-h UV-aged samples of (A) ITO-etched  $A_{HJ}$ , (B)  $Si_xN_y$ -etched  $B_{IBC}$ , and (C)  $Si_xN_y$ -etched  $D_{PERT}$ . (D) Spectral reflectance of test cell front surfaces, before (solid) and after (dashed) 2000 h of UV exposure testing:  $A_{HJ}$  (red),  $B_{IBC}$  (orange), and  $D_{PERT}$  (green)

the (p)a-Si and (i)a-Si layers and lower H concentration near the a-Si:H/c-Si interface and c-Si bulk. The loss of H near the a-Si:H/c-Si interface would indicate that there is less H available for passivation of dangling bonds or interfacial defect density, increasing carrier recombination and eventually decreasing  $V_{oc}$ . This is also consistent with the  $I$ - $V$  data for the HJ cell in Figure 4. Manzoor et al. showed that passivation of the c-Si surface with an intrinsic a-Si:H layer degrades over time under illumination.<sup>49</sup> This degradation is mostly due to an increase in interface defect density, which induces poor chemical passivation. Cho et al. also reported that HJ solar cells with a low H content have a poor a-Si:H/c-Si interface.<sup>50</sup> The deterioration of the interface is attributed to (i) voids created by insufficiently passivated c-Si surface dangling bonds, (ii) voids formed by  $\text{SiH}_2$  clusters, and (iii) Si particles caused by gas phase particle formation in silane plasma.

Another potential mechanism for UVID is chemical changes to the passivation layers, such as oxidation or stoichiometry. XPS is sensitive to changes in surface chemistry (chemical bond environment) and complements SIMS. To verify the chemical degradation mechanism, we acquired XPS depth profiles on the front surface of the cell at every 1 min of sputtering. The XPS spectra from the In 3d, O 1s, and Si 2p for  $\text{A}_{\text{HJ}}$  are shown in Figure S5. Only subtle differences were observed between the unaged and aged samples, suggesting that there are no major changes in the chemistry or bond configuration at the cell interfaces beyond the H measured by SIMS.

Finally, to further explore the source of UVID in the HJ cells, we performed optical reflectance measurements on the front surface of cells. Figure 5D shows that the difference in spectral reflectance between the unaged and UV-aged  $\text{A}_{\text{HJ}}$  cell is negligible ( $\Delta\rho_{\text{rs}} \approx 0.3\%$ ), suggesting that the front coatings are not significantly deteriorated. Combining the characterization results, we postulate that the damage to these HJ cells originates from the hydrogen effusion near the surface with subsequent migration into the bulk silicon, resulting in increased recombination loss.

### 3.2.2 | IBC cells

IBC cells display a small increase in power under both front- and rear-side exposures (2% and 6%, respectively, with uncertainty in the results of  $\pm 2\%$  and  $\pm 4\%$ , respectively) after UV aging, despite losses in  $I_{sc}$  and  $V_{oc}$  ( $-1\%$  to  $-2\%$ ). This anomalous behavior is attributed to the increase in  $FF$  ( $+3\%$  and  $+8\%$ , respectively). The reason for the increased  $FF$  is unclear, but it could be an artifact of flash  $I$ - $V$  testing or a result of changes in charge state induced by UV light. We did not explore the possible metastability of this performance gain in this work.

The SIMS profiles of the  $\text{B}_{\text{IBC}}$  cells are shown in Figure 7B. The H profiles (red) show an increased H concentration at or near the  $\text{Si}_x\text{N}_y/\text{SiO}_2$  interface and underneath the Si bulk after UV aging. It has been hypothesized that the energetic UV photons break the weak Si-H bonds, releasing hydrogen, which then diffuses toward the inner layers.<sup>47</sup> Hydrogen is crucial for defect passivation, but excess H

atoms could result in hydrogen-induced degradation.<sup>47</sup> By this mechanism,  $I_{sc}$  and  $V_{oc}$  losses can be attributed to extra H atoms forming H-clusters that cause increased carrier recombination. No significant differences were seen in the distribution of Si, O, and N profiles for the IBC cell. Similarly, the XPS spectra from the Si 2p, N 1s, and O 1s profiles (shown in Figure S6) demonstrated no significant differences after the UV exposure. Further, no major change was observed in the reflectance spectra at any wavelength. Taken together with the characterization results, we infer that the cause of damage to these IBC cells originates from the excess of H in c-Si. For these IBC cells, which are made of high-quality wafers, extra H atoms cannot further passivate defects, but do cause more degradation and compromise the performance.

### 3.2.3 | PERC and PERT cells

An interesting observation arises in p-PERC cell technologies. There is considerable variation in the extent of UVID in bifacial p-PERC cells between the front and rear sides. In these cells, the  $P_{max}$  decrease under front-side exposure lies in the narrow range of  $-1\%$  to  $-4\%$ , but reaches up to  $-13\%$  under rear-side exposure. The factors affecting the  $P_{max}$  decrease in p-PERC cells with rear-side exposure are  $I_{sc}$  and  $V_{oc}$  losses. The highest  $I_{sc}$  degradation ( $-10\%$ ) and  $V_{oc}$  loss ( $-3\%$ ) are seen in  $\text{J}_{\text{PERC}}$  cells. This is because bifacial p-PERC cells typically adopt different passivation schemes on the front and rear sides. The front surface of a bifacial PERC cell includes a selective phosphorous emitter (greater doping beneath the metal contacts) and a thin thermal oxide  $\text{SiO}_2$  passivation (ensuring low carrier recombination velocity), whereas the rear surface includes dielectric passivation of the  $\text{AlO}_x/\text{Si}_x\text{N}_y$  stack. We hypothesize that the lack of back surface field on the rear surface makes it more vulnerable to UV, as the rear instead relies on dielectric passivation from built-in charges within the  $\text{AlO}_x$  layer. Another important factor is the difference in optical performance (reflectance and absorptance, resulting from a different thickness and refractive index) of the hydrogenated  $\text{Si}_x\text{N}_y$  layer, which gives a different optical transfer function for the back of the cell. Generally, the  $\text{Si}_x\text{N}_y$  thickness on the rear side is greater than on the front side to improve passivation,<sup>51</sup> which would increase the absorption of UV photons. The variation in the refractive index also plays a vital role in cell degradation under UV exposure. Witteck et al. reported an increase in power loss with decreasing refractive index of the  $\text{Si}_x\text{N}_y$  layer during UV exposure.<sup>18</sup> It is evident that the  $\text{Si}_x\text{N}_y$  layer absorbs significant amounts of short-wavelength light, especially for films with a higher refractive index.<sup>52</sup> Typically, the rear  $\text{Si}_x\text{N}_y$  layer of the cell has a lower refractive index than the front  $\text{Si}_x\text{N}_y$  layer, thereby reducing reflectance and increasing the UV flux to the rear side. The concentration of H in the  $\text{Si}_x\text{N}_y$  layer, which may contribute to degradation, also varies with the refractive index.<sup>53</sup> The net effect of thickness and refractive index remains to be evaluated.

As shown in Figure 3, n-PERT cells from different manufacturers exhibited power degradation to varying extents after UV exposure. The  $P_{max}$  drop was greatest in  $\text{D}_{\text{PERT}}$  ( $-7\%$ ) and  $\text{C}_{\text{PERT}}$  ( $-3\%$ ), whereas



the  $E_{\text{PERT}}$  and  $F_{\text{PERT}}$  cells showed a slight improvement in power (2%). All of these cell types contain similar front passivation structures, thus, the variation in their UV sensitivity could be attributed to factors like differences in passivation layer deposition steps or the dopant concentration profiles of the front emitters. Furthermore, the bifacial  $D_{\text{PERT}}$  cells exhibited greater power degradation when irradiated on the rear side. The greater power loss is mostly correlated with the subsequent decreases in  $I_{\text{sc}}$  and  $V_{\text{oc}}$ , whereas the  $FF$  decrease is negligible, as shown in Figure 4B. In order to examine the underlying degradation mechanism, other characterizations like SIMS, XPS, and optical reflectance measurements were performed on this cell type.

The SIMS profiles of the  $D_{\text{PERT}}$  cells are shown in Figure 5C. Like in the IBC cells, the H profiles (red) show an increased H concentration at or near the  $\text{Si}_x\text{N}_y/\text{SiO}_2$  interface and underneath the Si bulk after UV aging. However, there are some changes in the Si, O, and N profiles of the n- $\text{PERT}$  cell that could have resulted from UV aging, which is verified by XPS and reflectance measurements. Figure 6 shows that the XPS spectra of the  $D_{\text{PERT}}$  cells are affected by UVID. The peak intensities of Si between the unaged and aged samples indicate a considerable increase in the concentration of silicon oxide, oxynitride, or intermediate suboxides at the  $\text{Si}_x\text{N}_y/\text{Si}$  interface after UV exposure. The N 1s peak also shows a slight shift toward higher binding energy with an increase in peak intensity, suggesting a greater amount of oxynitride in the  $\text{SiO}_x\text{N}_y$  composition. A similar chemical shift is exhibited in the O 1s peak, which supports the hypothesis that there is more oxygen content in the aged samples. We propose that UV irradiation of the  $D_{\text{PERT}}$  cell results in the formation of suboxides near the  $\text{Si}_x\text{N}_y/\text{Si}$  interface in the device. Such defects are known to decrease the carrier lifetime and cell efficiency.<sup>54</sup> This hypothesis of interfacial oxidation in the aged samples is consistent with the  $I$ - $V$

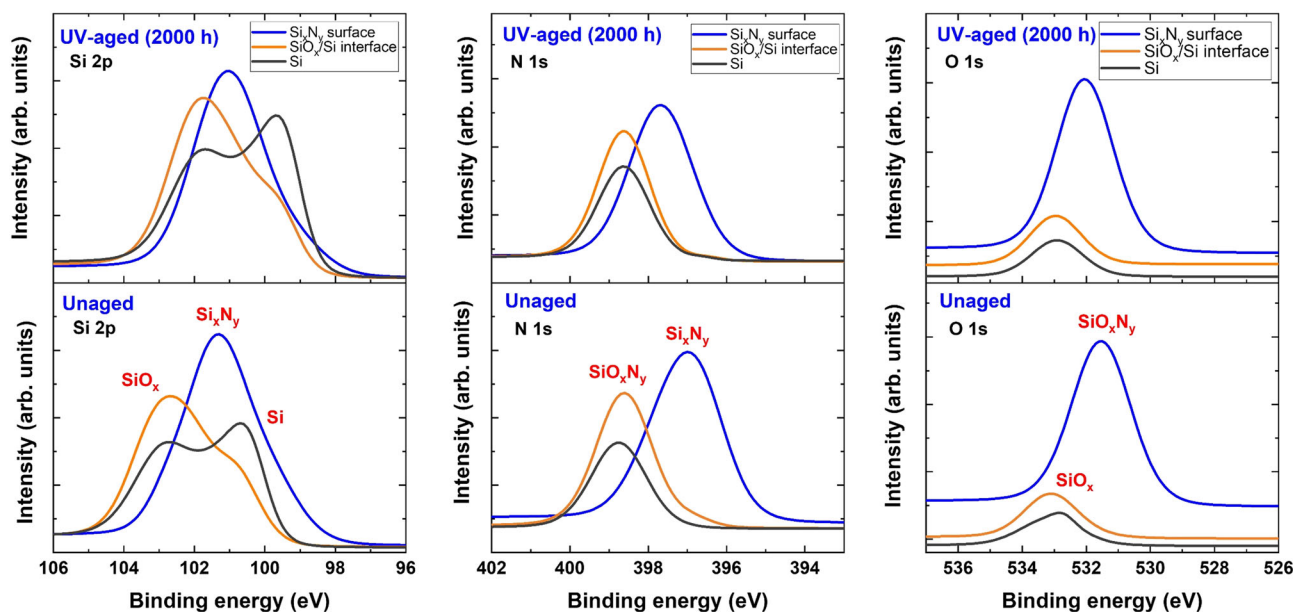
results—greater  $I_{\text{sc}}$  and  $V_{\text{oc}}$  losses after UV exposure. According to Black et al, the suboxides and oxygen vacancies in the oxide layer are the preferential sites where the charged state of hydrogen (or protons) are trapped and form positively charged centers.<sup>55</sup> The photoinjected electrons could knock out the protons and subsequently migrate along the interface to depassivate Si-H bonds and increase defect generation. For the IBC cell, this energy could easily be supplied by the electrons injected from Si by UVA-340 lamp exposure. It should be noted that the oxygen availability in an encapsulated module would be less, limiting degradation occurring through oxidation—although any monolayer effects at the passivation/Si interface would require minimal oxygen.

Figure 5D shows a nearly 1% increase in the representative solar-weighted reflectance of photon irradiance ( $\rho_{\text{rsw}}$ ) of the aged  $D_{\text{PERT}}$  sample, occurring mostly in the spectral range of 240–500 nm. The  $\rho_{\text{rsw}}$  is similar to the representative solar-weighted characteristic for transmittance in Miller et al.<sup>48</sup> and can be expected to give a ~1% decrease in the photocurrent generation. This is approximately half of the  $I_{\text{sc}}$  loss (−2.3%) and the subsequent  $P_{\text{max}}$  loss in the  $D_{\text{PERT}}$  cell (Figure 3). Based on the XPS data, the change in  $\rho_{\text{rsw}}$  is caused by chemical changes near the  $\text{Si}_x\text{N}_y$  passivating layer/Si interfacial region.

By comparing composition and optical performance, we observed both the chemical and physical changes causing the current loss and increased recombination activity at the Si/passivation interface.

### 3.2.4 | BSF cells

Of further interest is the superior performance and durability of the conventional Al-BSF cells against UVID; these cells exhibited



**FIGURE 6** High-resolution XPS spectra obtained on the front surfaces of UV-aged (for 2000 h) and unaged  $D_{\text{PERT}}$  samples for Si 2p, N 1s, and O 1s. Profiles are shown at three regions: the  $\text{Si}_x\text{N}_y$  surface,  $\text{SiO}_x/\text{Si}$  interface, and Si bulk. The peak intensity is normalized to that of the unaged sample

the least degradation in each  $I$ - $V$  parameter. The front and rear surfaces of these cells are typically passivated by establishing built-in electric field results from the spatially non-uniform concentration of the dopant atoms in the crystal lattice. This creates a high-low junction ( $n^+p$  in the front or  $p^+p$  in the rear) that repels the minority carriers to limit both the surface and bulk recombination losses. We hypothesize that the front surface field and complete blocking of UV irradiation by the Al on the rear helps reduce the UV sensitivity of the surface recombination velocity in Al-BSF cells. Modern high-efficiency cell technologies have reduced the surface field associated with higher sheet resistance, for example, with the use of selective emitters and more reliance on passivation based on termination of surface dangling bonds and charges within the dielectric layers that can achieve reduced recombination currents.<sup>56–58</sup> Cell types with these surface passivation destabilized by UV irradiation do not have the benefit of as large an extent of surface field for resistance to UVID.

### 3.3 | UVID and hot-electron damage

The UV testing was carried out at  $\sim 2.5\times$  UV suns, that is, modestly concentrated sunlight that may enable hot-electron damage in the cells, as mentioned in the introduction section. PV installations, however, are operated at  $1\times$  UV sun, which may limit hot-electron damage. To study the influence of electron photoinjection on hot-carrier damage, select cell technologies (HJ, n-PERT, and p-PERC) were subjected to UV irradiation from the front side of the cell in a short-circuit configuration. The selection of the cells for the open-circuit and short-circuit studies was undertaken prior to starting the experiment, a few criteria such as availability of cells and variety of cells in the test, were considered. Figure 7 shows the change in  $I$ - $V$  parameters for cells illuminated under open-circuit and short-circuit conditions. The majority of short-circuited cells (shown in red) exhibited greater power loss than the open-circuited cells (shown in black). Uniquely, the  $P_{max}$  loss of  $A_{HJ}$  cells was greater under the short-circuit condition

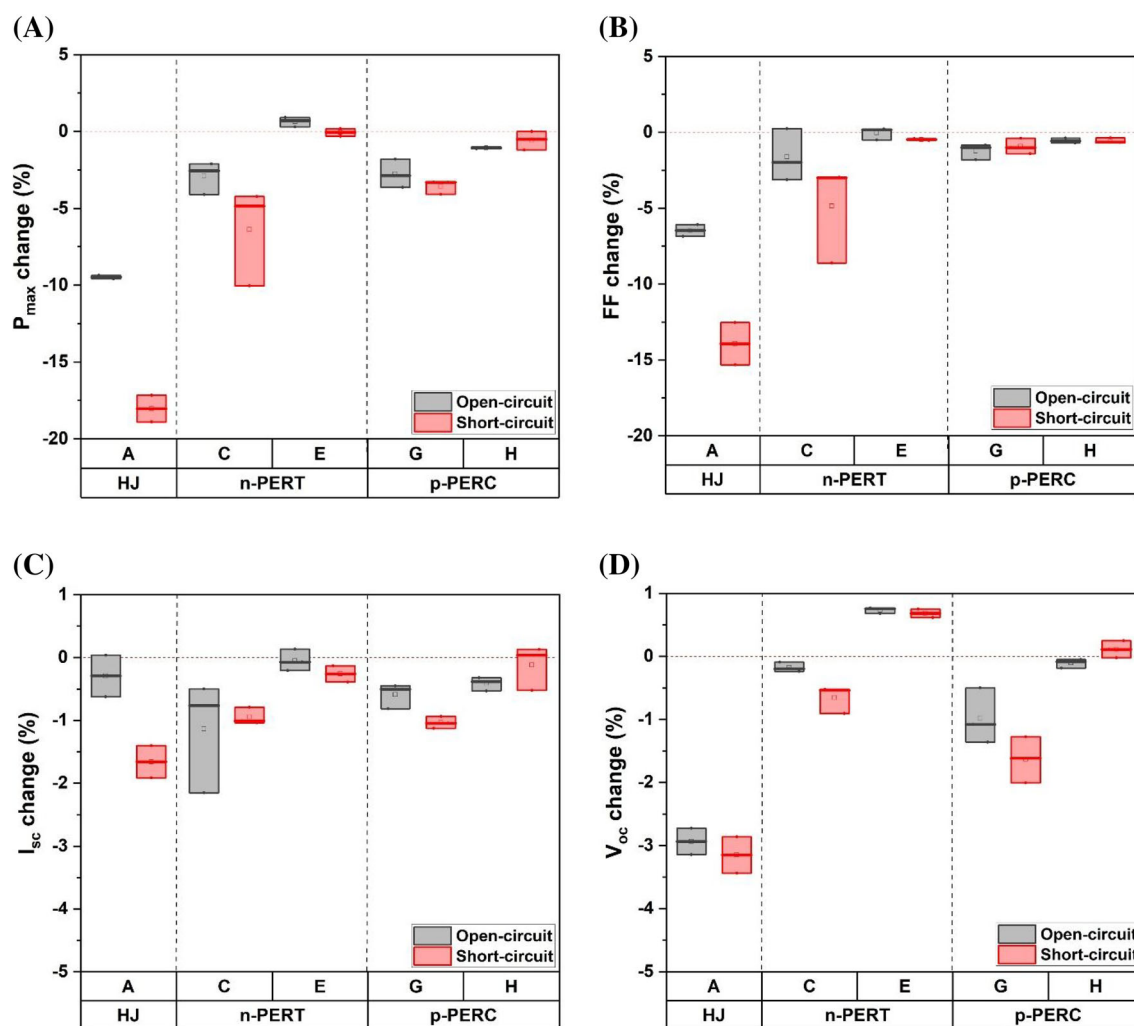


**FIGURE 7** Change in  $I$ - $V$  parameters of the test cells after 2000 h of UV exposure on the front side, color-coded by electrical load configuration (black = open-circuit; red = short-circuit). The  $I$ - $V$  measurements were done by illuminating the front sides of the cells. As a guide to the eye, a 0% change is indicated by a red dotted line

(−18%) than under the open-circuit condition (−9%), which was caused by the combined losses in  $I_{sc}$  (−1.7%),  $V_{oc}$  (−3.1%), and  $FF$  (−14%). Another cell type,  $C_{PERT}$ , showed a power decrease of −7%; by contrast, the change in  $E_{PERT}$  cells was insignificant (less than 1%). On the other hand,  $G_{PERC}$  and  $H_{PERC}$  cells exhibited  $P_{max}$  degradation of −4% and −1%, respectively, suggesting that PERC cells are less susceptible to hot-carrier damage. The data indicates that the hot-carrier injection can also occur under the open-circuit condition, but more concentrated sunlight is required to cause a similar effect.

Here, we have identified different degradation mechanisms based on representative examples of different silicon PV cell technologies; however, their occurrence depends on the details of the cell make, including manufacturing processing (time, temperature, and other parameters), dopant (concentration and depth profiles), and thin-film layers (including their thickness and the use of interlayers). No single complete degradation model is developed here; instead, this study indicates that multiple models are required and further clarifies the enabling mechanisms (loss of hydrogen, oxidation, and hot-carrier damage).

### 3.4 | UVID in PV modules using spectral optical analysis

We used a spectrum-based analysis, where the absorption of each layer and the reflectance<sup>59</sup> at each interface are quantified, to understand the interaction of UV light with the module materials. Based on this analysis, we assessed if the relative rate of damage between the  $Si_xN_y$  layer and the  $Si_xN_y/Si$  interface of c-Si cells. Figure 8 provides a cross-sectional schematic of a PV module, highlighting the travel path

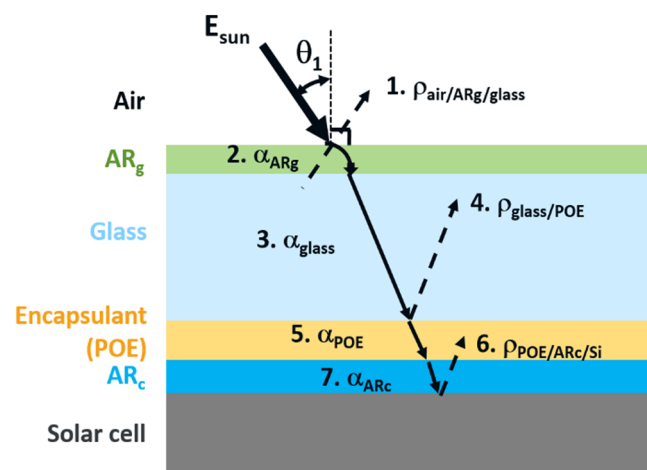


**FIGURE 8** Cross-sectional schematic of a PV module, showing the various optical interactions—absorptance ( $\alpha$ ) and reflectance ( $\rho$ )—of incident sunlight through the different interfaces, materials, and material stacks. The absorptance of the Si cell and reflectance from the back surface of the cell are not shown because less than 1% of the incident light reaches the Si below 353 nm (for UV-blocking encapsulant) or below 302 nm (for UV-transmitting encapsulant)

of incident sunlight and its interactions with the module materials. The absorptances  $\alpha_{ARg}$ ,  $\alpha_{glass}$ ,  $\alpha_{POE}$ , and  $\alpha_{ARc}$  represent the bulk absorptance in the antireflective coating of glass, the bulk glass, the polyolefin (POE) encapsulant, and the antireflective coating on the cell, respectively. The reflectances  $\rho_{glass/POE}$  and  $\rho_{POE/ARc/Si}$  represent the reflectance at the encapsulant interfaces with the front glass and the cell, respectively. The optical interactions 1 and 6 in Figure 8 represent the reflectances at the bulk/thin-film/bulk material stack. The corresponding optical absorptance and reflectance are shown in Figure 9 (bottom); the source spectra of the UVA-340 fluorescent lamp used in our UV test experiment and the spectra of the sun (AM1.5G, from IEC 60904-3) for the spectral range of 250–500 nm are shown in Figure 9 (top). We also assessed the benefits of UV-blocking encapsulants in mitigating the impact of UVID and increasing cell performance. For analytical modeling, we considered the optical response of textured Solite glass (coated with a porous silica  $AR_g$ ), UV-transparent and UV-blocking POE encapsulants,  $AR_c$  solely composed of  $Si_xN_y$ , and a silicon solar cell. Only the initial performance of the packaging materials is considered in the model and the effects of

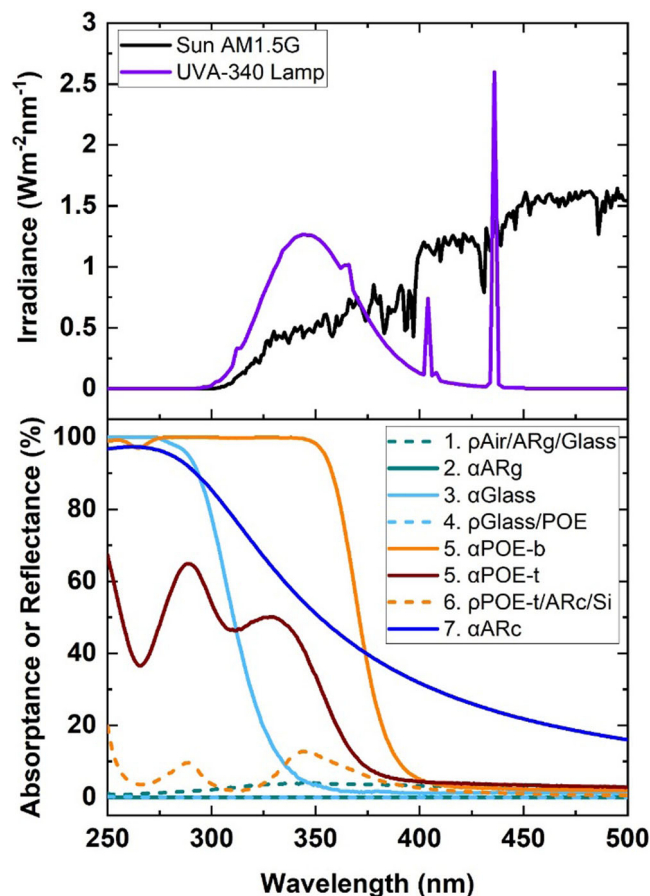


**FIGURE 9** Spectra of the sun and the UV-340 lamp used in the UV screen test (top). Representative spectra of different optical interactions affecting performance in an encapsulated PV module (bottom). Reflectance ( $\rho$ ) at interfaces and stacks and absorptance ( $\alpha$ ) in materials are represented by dashed and solid curves, respectively

aging over time are not considered at this time. For example, continued solarization of the glass would reduce UV flux to the cell, discoloration of the encapsulant would reduce UV flux to the cell, reduction in the crystallinity of the encapsulant would increase UV flux to the cell, and the net effect of damage to the AR<sub>c</sub> is unknown.

From the spectral analysis of Figure 9, we determined that for a PV module, the incident UV sunlight is most attenuated by the Si<sub>x</sub>N<sub>y</sub> AR<sub>c</sub>, then the encapsulant, and then the front glass, respectively. In the case of UV-transparent POE (POE-t), the UV photons are predominantly absorbed in the bulk of AR<sub>c</sub> (i.e., a Si<sub>x</sub>N<sub>y</sub> layer); few photons reflect off of the encapsulant/AR<sub>c</sub>/Si stack. The optical interaction within a PV module constructed with POE-t would be expected to facilitate bond breakage of Si-H at the Si<sub>x</sub>N<sub>y</sub>/Si interface by UV radiation, enabling H to diffuse into the Si bulk. This accounts for greater damage in the modules that contain UV-transmitting encapsulants. However, UV-blocking POE (POE-b) can absorb a substantial portion of UV flux below 360 nm before it reaches the Si<sub>x</sub>N<sub>y</sub> layer, preventing UV degradation.

In addition to the multiple degradation mechanisms identified in the composition analysis, the optical performance of the AR<sub>c</sub> makes UVID further sensitive to the cell construction. In Figure 9, changes in the composition and density (refractive index) and thickness (including manufacturing variability) of the AR<sub>c</sub> would greatly affect the UV dose at the Si interface. It may be that no single critical wavelength exists due to different damage mechanisms and UV doses encountered with today's variety of PV cells.

Next, we estimated the UV dose for the UV screen test on bare cells relative to that of a PV module operating outdoors. Table 2 provides the UV intensity at the wavelength of 340 nm, incident at either the encapsulant/Si<sub>x</sub>N<sub>y</sub> interface or the Si<sub>x</sub>N<sub>y</sub>/Si interface. Values are given for a bare cell and a PV module encapsulated with a UV-transparent or a UV-blocking POE. Figure 9 and Table 2 remind us that the UVA-340 lamps produced higher irradiance levels relative to the terrestrial sun below about 370 nm. Comparing the UVA intensity of the lamp and the sun at 340 nm confirms an acceleration factor (AF) of 2.5 on a W·m<sup>-2</sup> basis in our UV screen test relative to AM1.5G. The spectral analysis, which is based on absorbance/reflectance interactions of incident flux with different material layers of a PV module (Figure 9), shows that the UV intensity at the Si<sub>x</sub>N<sub>y</sub>

layer is attenuated by a factor of 2 in a module compared with a bare cell. Together, the intensity and transfer of radiation give a net AF of ~5×, which may be used to compare the degradation of the bare cells in our study to the expected results for a fielded module. Using the net AF, the average degradation rate of -0.6%·year<sup>-1</sup> obtained in the UV aging test on unpackaged cells is translated to -0.12%·year<sup>-1</sup> for an encapsulated module in outdoor conditions, with a corresponding maximum degradation rate of -0.73%·year<sup>-1</sup>. This is comparable to aggregated published mean degradation rates of c-Si PV modules, which are in the range of -0.5%·year<sup>-1</sup> to -1.1%·year<sup>-1</sup>. The analytical calculations in Table 2 also show that UV-blocking encapsulants can reduce UV transmission by an additional factor of ~50. The aforementioned analysis does not consider wavelength sensitivity—for example, if the UVID degradation has a nonlinear action spectrum for damage.<sup>40</sup>

## 4 | POTENTIAL UVID MITIGATION SOLUTIONS

The negative impact of UVID can be minimized through changes in module packaging materials and/or cell design. Historically, PV encapsulants were formulated with suitable additives of varying UV-blocking abilities. Industry product formulations such as benzophenone- or benzotriazole-based UV absorbers have their characteristic absorption peaks at wavelengths of 280–380 nm,<sup>60</sup> which allow photon wavelengths greater than 360 nm to reach the cell surface. Recent advancements have led to an improved understanding of modern encapsulant formulations, which allow for a more tailored UV cut-off wavelength compared to old formulations. For example, triazine-based additives might be used to shift the UV absorbance to the spectral range of 260–280 nm,<sup>32</sup> decreasing the UV cut-off wavelength below 360 nm. Multiple UV absorbers may also be used in the formulation to further tailor the spectral range of optical transmittance of the encapsulant. The raw materials cost of a UV absorber made using industry encapsulant formulations is currently estimated to be in the range of \$0.05–\$0.2·m<sup>-2</sup>. The consequences of using a UV absorber include possible discoloration of the encapsulant and a reduction in performance from the chromophore species.<sup>61</sup> To justify

**TABLE 2** UV intensity factor calculations for different PV applications

Application	Sample	UVA intensity (W·m <sup>-2</sup> nm <sup>-1</sup> at 340 nm)	Acceleration factor
Reference	Terrestrial sun (AM1.5G)	0.5	1.0
Accelerated UV test, bare cells	UVA-340 lamp	1.24	2.5
	UVA-340/air/Si <sub>x</sub> N <sub>y</sub>	0.77	1.5
	UVA-340/air/Si <sub>x</sub> N <sub>y</sub> /Si	0.074	0.15
Outdoor, PV module	sun/air/AR <sub>g</sub> /glass/POE-b/Si <sub>x</sub> N <sub>y</sub>	0.0078	0.016
	sun/air/AR <sub>g</sub> /glass/POE-t/Si <sub>x</sub> N <sub>y</sub>	0.37	0.74
	sun/air/AR <sub>g</sub> /glass/POE-b/Si <sub>x</sub> N <sub>y</sub> /Si	0.00068	0.0014
	sun/air/AR <sub>g</sub> /glass/POE-t/Si <sub>x</sub> N <sub>y</sub> /Si	0.032	0.064

Note: The acceleration factor is the ratio of UVA intensity at 340 nm at a specific material interface (or stack) in the cell (or module) to that of the sun.



the use of a UV absorber, the cost of the absorber and the resulting loss of electricity production from any potential discoloration it may cause needs to be less than the cost of the loss of electricity production from UVID.

Other solutions for mitigating UVID in encapsulated PV modules include using a specialized glass cover, such as cerium-containing glass, advantageously solarized glass, or antireflective coatings tailored to reduce UV transmittance. Previous studies have confirmed the ability of Ce-doped glass to reduce discoloration of ethylene-co-vinyl acetate (EVA).<sup>62,63</sup> The UV-blocking ability of Ce glass is expected to protect solar cells from the damaging effects of UVID. However, its utility is limited due to energy-intensive processes, the high cost of production, and poor recyclability. The presence of rare-earth elemental impurities in the glass makes the entire recycling process less economically viable for the PV industry due to costly reducing agents for dissolution and the complexity of the metal extraction processes.<sup>64</sup> A second method to induce desirable changes in the glass material is solarization, in which a glass is exposed to either sunlight or artificial light sources for extended periods. King et al. demonstrated a ~2% loss in solar-weighted transmittance (>800 nm) as well as an increase in absorption in the 330–400 nm region of the UV spectrum for 0.2 wt.% Ce-containing float glass after several hours of solarization under highly concentrated, full-spectrum solar radiation above 1000 suns, with sample temperatures maintained below 100°C. The incident photon dose was equivalent to 8 years outdoors in Golden, Colorado, USA.<sup>65</sup> Here, Ce acts as a solarization agent because the  $\text{Ce}^{3+}$  state initially present in the glass is oxidized to the  $\text{Ce}^{4+}$  state under prolonged light exposure. Ce is no longer used in the PV industry, but Mn and Sb are often added to soda-lime glass for whitening and improvement of transmittance.<sup>66</sup> The redox reaction between Mn and Sb advantageously results in solarization that reduces UV transmittance, but typically on the order of a few nanometers. Antireflective coatings, which immediately improve electricity generation on the order of a few percent, have found widespread use in PV since around 2005.<sup>67</sup> The currently popular graded-index coatings using porous silica do not affect UV transmittance greatly. However, the destructive interference coatings that use layers of metal oxide films give a greater reduction.<sup>67</sup> Ideally, a multilayer coating could be designed to both reduce UV transmittance and reject spurious infrared wavelengths (to improve module performance relative to its temperature coefficient). The adoption of multilayer coatings for PV would depend on cost reduction, widespread use and economies of scale, and/or the need for more durable  $\text{AR}_g$  coatings in soiling-prone locations.

On the cell side, modifications to passivation schemes can help mitigate UVID. For instance, the  $\text{Si}_x\text{N}_y$  antireflective coating with a refractive index of greater than 2.3 was found to decrease the degradation rate.<sup>53</sup> With the increase in refractive index, the UV absorption in the  $\text{Si}_x\text{N}_y$  layer also increases, which in turn reduces the number of UV photons reaching the  $\text{Si}_x\text{N}_y/\text{Si}$  passivation interface. This reduces damage, but also leads to a non-negligible loss in photocurrent, to the extent that the UV absorption continues into the blue wavelengths. Further, cells featuring  $\text{AlO}_x/(\text{p}^+)\text{Si}$  passivation are more UV-stable

than those with a  $\text{Si}_x\text{N}_y$  passivation layer.<sup>21</sup> This could be due to the formation of a stable interfacial  $\text{SiO}_x$  layer between Si and  $\text{AlO}_x$ <sup>31,68</sup> and an increase in negative fixed charges within the  $\text{AlO}_x$  layer under UV illumination.<sup>69</sup> These factors improve the passivation, which in turn increases the module power output. The most durable among high-efficiency cell technologies (HJ, IBC, PERC, or PERT) remains to be proven for a wide variety of makes and models of cells.

## 5 | CONCLUSIONS

In this study, we demonstrate the UV susceptibility of various modern PV cell designs through an accelerated UV exposure test on unencapsulated silicon solar cells, including bifacial cells. High-efficiency modern cell technologies, including HJ (–11%), n-PERT (–3% to –7%), and p-PERC (–1% to –4%) showed greater  $P_{\text{max}}$  losses compared to conventional Al-BSF cells (–1%). We found the rear sides of bifacial cells to be more vulnerable to UVID than the front sides, which could be attributed to differences in the surface field and passivation schemes used on the front versus rear sides. As the  $I$ - $V$  results show, different cell technologies underwent different degradation mechanisms. Power loss in HJ cells was dominated by a significant drop in  $V_{\text{oc}}$  and  $FF$ , whereas IBC, n-PERT, and p-PERC cell technologies exhibited greater  $I_{\text{sc}}$  and  $V_{\text{oc}}$  losses. SIMS characterization showed that UVID is related to hydrogen redistribution in the cell. After UV exposure, higher H concentration was seen near the passivation/Si interface and Si bulk, where bond breaking of hydrogen that passivated the cell surface led to excess H atom clusters that facilitated carrier recombination and deteriorated the cell performance. A separate degradation mechanism (e.g., oxidation at Si interface) was identified for one of the n-PERT cells using XPS and optical reflectance characterization. UV exposure under a short-circuit configuration of a cell seems to induce greater power degradation than an open-circuit configuration, suggesting a third mechanism related to the hot-carrier injection.

The optical modeling of spectral interactions at c-Si module layers and their interfaces demonstrated attenuation of UV radiation by absorbance in the  $\text{Si}_x\text{N}_y$  bulk and reflectance by the encapsulant/ $\text{Si}_x\text{N}_y/\text{Si}$  stack. The optical performance of the  $\text{AR}_c$  makes UVID further sensitive to the cell construction, as its composition, density, and thickness affect the damage susceptibility and rate of degradation. For our experiment, we determined an acceleration factor of  $2.5\times$  based on the intensity and possible reciprocity of the UV lamp, and an additional acceleration of  $2\times$  between the bare cell specimens examined in this study and a fielded PV module. Using this correlation, we estimated average and maximum power degradation rates of  $-0.12\%\cdot\text{year}^{-1}$  and  $-0.73\%\cdot\text{year}^{-1}$ , respectively, for a PV module containing UV-transmitting encapsulant. Although we demonstrated that UVID reduces the overall power output of modern cell technologies, including higher degradation rates on the back of bifacial cells, these effects may be mitigated by tailoring the UV-blocking characteristics of new encapsulant formulations, using spectral-specific antireflective coatings, and developing UV-stable PV cell designs.

## ACKNOWLEDGEMENTS

The authors are grateful to André F. R. Augusto, Stanislaw Herasimenka, Som Dahal, Pradeep Balaji, and Stuart Bowden of Arizona State University (ASU); Afshin Andreas and Paul Ndione of NREL; Wei Luo of Solar Energy Research Institute of Singapore (SERIS); Katherine Han of SunPower Corp.; Lizhong Mao and Jean-Nicolas Jaubert of Canadian Solar; Qi Wang and Lin Zhang of Jinko Solar; Brian Habersberger of Dow Chemical; and Sari-Beth Samuels of Solvay.

This work was authored in part by the National Renewable Energy Laboratory, operated by Alliance for Sustainable Energy, LLC, for the U.S. Department of Energy (DOE) under Contract No. DE-AC36-08GO28308. Funding provided as part of the Durable Modules Materials Consortium (DuraMAT), an Energy Materials Network Consortium funded by the U.S. Department of Energy (DOE), Office of Energy Efficiency and Renewable Energy, Solar Energy Technologies Office agreement number 32509. Part of this work was performed at the Stanford Nano Shared Facilities (SNSF), supported by the National Science Foundation under the award ECCS-2026822. We also thank EAG Laboratories, New Jersey, USA, for conducting the SIMS measurements.

The U.S. Government retains and the publisher, by accepting the article for publication, acknowledges that the U.S. Government retains a nonexclusive, paid-up, irrevocable, worldwide license to publish or reproduce the published form of this work, or allow others to do so, for U.S. Government purposes.

## CONFLICT OF INTEREST

The authors declare no conflict of interest. The views expressed in the article do not necessarily represent the views of the DOE or the U.S. Government.

## AUTHOR CONTRIBUTIONS

*Study concept and design:* Peter Hacke, Laura Schelhas, and David Miller. *Writing original draft:* Archana Sinha, David Miller. *Experimental testing and characterization:* Kent Terwilliger, Jiadong Qian, Archana Sinha, Stephanie Moffitt, David Miller, Peter Hacke, and Katherine Hurst. *Data analysis and interpretation:* Peter Hacke, David Miller, Archana Sinha, and Laura Schelhas. *Optical model:* David Miller. *Study supervision:* Peter Hacke and Laura Schelhas.

## DATA AVAILABILITY STATEMENT

The data that support the findings of this study are available in the supporting information of this article.

## ORCID

Archana Sinha  <https://orcid.org/0000-0001-5272-1123>

David C. Miller  <https://orcid.org/0000-0002-4698-5277>

Laura T. Schelhas  <https://orcid.org/0000-0003-2299-1864>

Peter Hacke  <https://orcid.org/0000-0003-4850-0947>

## REFERENCES

- Jordan DC, Kurtz SR, VanSant K, Newmiller J. Compendium of photovoltaic degradation rates. *Prog Photovoltaics Res Appl.* 2016;24(7): 978-989. doi:10.1002/pip.2744
- Stein JS, Robinson C, King B, Deline C, Rummel S, Sekulic B. PV lifetime project: measuring PV module performance degradation: 2019 indoor flash testing results. 2019.
- Miller DC, Annigoni E, Ballion A, et al. Degradation in PV encapsulation transmittance: an interlaboratory study towards a climate-specific test. In 2015 IEEE 42nd Photovoltaic Specialist Conference (PVSC), Jun. 2015, pp. 1-6. doi:10.1109/PVSC.2015.7355607
- Wohlgemuth JH, Kempe MD, Miller DC. Discoloration of PV encapsulants. In 2013 IEEE 39th Photovoltaic Specialists Conference (PVSC), Jun. 2013, pp. 3260-3265. doi:10.1109/PVSC.2013.6745147
- Gopalakrishna H, Arularasu P, Dolia K, Sinha A, Tamizhmani G. Characterization of encapsulant degradation in accelerated UV stressed mini-modules with UV-cut and UV-pass EVA. In 2019 IEEE 46th Photovoltaic Specialists Conference (PVSC), Jun. 2019, pp. 1961-1964. doi:10.1109/PVSC40753.2019.8980897
- Dunn L, Gostein M, Stueve B. Literature review of the effects of UV exposure on PV modules. In NREL PV module reliability workshop, 2013, pp. 1-19.
- Yuen PY, Moffitt SL, Novoa FD, Schelhas LT, Dauskardt RH. Tearing and reliability of photovoltaic module backsheets. *Prog Photovoltaics Res Appl.* 2019;27(8):693-705. doi:10.1002/pip.3144
- Liu F. *Ultra-Violet Degradation Behavior of Polymeric Backsheets for Photovoltaic Modules*. North Dakota State University; 2013. doi:10.4324/9781315721606-101
- Gruenbaum PE, Sinton RA, Swanson RM. Light-induced degradation at the silicon/silicon dioxide interface. *Appl Phys Lett.* 1988;52(17): 1407-1409. doi:10.1063/1.99130
- Gruenbaum PE, Sinton RA, Swanson RM. Stability problems in point contact solar cells. In Conference Record of the Twentieth IEEE Photovoltaic Specialists Conference, 1988, pp. 423-428. doi:10.1109/PVSC.1988.105736
- Gruenbaum PE, Gan JY, King RR, Swanson RM. Stable passivations for high-efficiency silicon solar cells. In IEEE Conference on Photovoltaic Specialists, 1990, pp. 317-322. doi:10.1109/PVSC.1990.111639
- Verlinden PJ, Swanson RM, Crane RA. High efficiency silicon point-contact solar cells for concentrator and high value one-sun applications. In 12th European Photovoltaic Solar Energy Conference and Exhibition, 1994, pp. 1477-1480.
- Lauinger T, Moschner J, Aberle AG, Hezel R. Optimization and characterization of remote plasma-enhanced chemical vapor deposition silicon nitride for the passivation of p-type crystalline silicon surfaces. *J Vac Sci Technol A.* 1998;16(2):530-543. doi:10.1116/1.581095
- Aberle AG, Hezel R. Progress in low-temperature surface passivation of silicon solar cells using remote-plasma silicon nitride. *Prog Photovoltaics Res Appl.* 1997;5(1):29-50. doi:10.1002/(SICI)1099-159X(199701/02)5:1%3C29::AID-PIP149%3E3.0.CO;2-M
- Kamioka T, Takai D, Tachibana T, Kojima T, Ohshita Y. Plasma damage effect on ultraviolet-induced degradation of PECVD SiNx:H passivation. In 2015 IEEE 42nd Photovoltaic Specialist Conference (PVSC), Jun. 2015, pp. 1-3. doi:10.1109/PVSC.2015.7356326
- Tachibana T, Takai D, Kojima T, Kamioka T, Ogura A, Ohshita Y. Minority carrier recombination properties of crystalline defect on silicon surface induced by plasma enhanced chemical vapor deposition. *ECS J Solid State Sci Technol.* 2016;5(9):Q253-Q256. doi:10.1149/2.0371609jss
- Cicero RL, Linford MR, Chidsey CED. Photoreactivity of unsaturated compounds with hydrogen-terminated silicon(111). *Langmuir.* 2000; 16(13):5688-5695. doi:10.1021/la9911990
- Witteck R, Schulte-Huxel H, Veith-Wolf B, et al. Reducing UV induced degradation losses of solar modules with c-Si solar cells featuring dielectric passivation layers. In 2017 IEEE 44th Photovoltaic Specialist Conference (PVSC), 2017, pp. 1366-1370. doi:10.1109/PVSC.2017.8366019

19. Park SH, Ahn SJ, Gwak J, et al. Effectiveness of full spectrum light soaking on solar cell degradation analysis. *Curr Appl Phys*. 2013;13(8):1684-1688. doi:[10.1016/j.cap.2013.06.011](https://doi.org/10.1016/j.cap.2013.06.011)
20. Witteck R, Jäger P, Rudolph M, et al. UV-stable surface passivation for crystalline silicon cells in solar modules with UV light transmitting encapsulation materials. In 2019 IEEE 46th Photovoltaic Specialists Conference (PVSC), Jun. 2019, pp. 2238-2242. doi:[10.1109/PVSC40753.2019.8980612](https://doi.org/10.1109/PVSC40753.2019.8980612)
21. Witteck R, Min B, Schulte-Huxel H, et al. UV radiation hardness of photovoltaic modules featuring crystalline Si solar cells with  $\text{AlO}_x/\text{p}^+$ -type Si and  $\text{SiN}_x/\text{n}^+$ -type Si interfaces. *Phys Status Solidi Rapid Res Lett*. 2017;11(8):1700178. doi:[10.1002/pssr.201700178](https://doi.org/10.1002/pssr.201700178)
22. Osterwald CR, Anderberg A, Rummel S, Ottoson L. Degradation analysis of weathered crystalline-silicon PV modules. In Conference Record of the Twenty-Ninth IEEE Photovoltaic Specialists Conference, 2002, 2002, pp. 1392-1395. doi:[10.1109/PVSC.2002.1190869](https://doi.org/10.1109/PVSC.2002.1190869)
23. Ruby DS, Schubert WK. The effects of concentrated ultraviolet light of high-efficiency silicon solar cells. In The Conference Record of the Twenty-Second IEEE Photovoltaic Specialists Conference - 1991, 1991, pp. 111-117. doi:[10.1109/PVSC.1991.169192](https://doi.org/10.1109/PVSC.1991.169192)
24. Lauinger T, Moschner J, Aberle AG, Hezel R. UV stability of highest-quality plasma silicon nitride passivation of silicon solar cells. In Conference Record of the Twenty Fifth IEEE Photovoltaic Specialists Conference - 1996, 1996, pp. 417-420. doi:[10.1109/PVSC.1996.564032](https://doi.org/10.1109/PVSC.1996.564032)
25. Jin H, Li N, Zhang X, Wang Q. The development and research of PVQAT TG13. 2018.
26. Lindroos J, Savin H. Review of light-induced degradation in crystalline silicon solar cells. *Sol Energy Mater Sol Cells*. 2016;147:115-126. doi:[10.1016/j.solmat.2015.11.047](https://doi.org/10.1016/j.solmat.2015.11.047)
27. Niewelt T, Schon J, Warta W, Glunz SW, Schubert MC. Degradation of crystalline silicon due to boron-oxygen defects. *IEEE J Photovoltaics*. 2017;7(1):383-398. doi:[10.1109/JPHOTOV.2016.2614119](https://doi.org/10.1109/JPHOTOV.2016.2614119)
28. Kersten F, Engelhart P, Ploigt HC, et al. A new mc-Si degradation effect called LeTID. In 2015 IEEE 42nd Photovoltaic Specialist Conference (PVSC), 2015, pp. 1-5. doi:[10.1109/PVSC.2015.7355684](https://doi.org/10.1109/PVSC.2015.7355684)
29. Sio HC, Wang H, Wang Q, et al. Light and elevated temperature induced degradation in p-type and n-type cast-grown multicrystalline and mono-like silicon. *Sol Energy Mater Sol Cells*. 2018;182:98-104. doi:[10.1016/j.solmat.2018.03.002](https://doi.org/10.1016/j.solmat.2018.03.002)
30. Werner F, Schmidt J. Manipulating the negative fixed charge density at the c-Si/ $\text{Al}_2\text{O}_3$  interface. *Appl Phys Lett*. 2014;104(9):091604. doi:[10.1063/1.4867652](https://doi.org/10.1063/1.4867652)
31. Werner F, Veith B, Zielke D, et al. Electronic and chemical properties of the c-Si/ $\text{Al}_2\text{O}_3$  interface. *J Appl Phys*. 2011;109(11):113701. doi:[10.1063/1.3587227](https://doi.org/10.1063/1.3587227)
32. Tachibana T, Takai D, Yamashita Y, et al. Effects of texture structure on crystalline damage induced by  $\text{SiN}_x$  plasma CVD. In 29th European Photovoltaic Solar Energy Conference and Exhibition, 2014, pp. 1090-1091. doi:[10.4229/EUPVSEC20142014-2AV.3.49](https://doi.org/10.4229/EUPVSEC20142014-2AV.3.49)
33. Gruenbaum PE, King RR, Swanson RM. Photoinduced hot-electron damage in silicon point-contact solar cells. *J Appl Phys*. 1989;66(12):6110-6114. doi:[10.1063/1.343592](https://doi.org/10.1063/1.343592)
34. Gruenbaum PE, Gan JY, Swanson RM. Use of ultrathin oxides and thin polycrystalline silicon films for stable high-efficiency silicon solar cells. *Appl Phys Lett*. 1991;58(9):945-947. doi:[10.1063/1.104486](https://doi.org/10.1063/1.104486)
35. Buchanan DA, Marwick AD, DiMaria DJ, Dori L. Hot-electron-induced hydrogen redistribution and defect generation in metal-oxide-semiconductor capacitors. *J Appl Phys*. 1994;76(6):3595-3608. doi:[10.1063/1.357420](https://doi.org/10.1063/1.357420)
36. ATLAS material testing solutions. <http://atlas-mts.com/knowledge-center/data-and-tools/weathersummaryreports>
37. Habte A, Sengupta M, Gueymard CA, Narasappa R, Rosseler O, Burns DM. Estimating ultraviolet radiation from global horizontal irradiance. *IEEE J Photovoltaics*. 2019;9(1):139-146. doi:[10.1109/JPHOTOV.2018.2871780](https://doi.org/10.1109/JPHOTOV.2018.2871780)
38. Gueymard CA. Parameterized transmittance model for direct beam and circumsolar spectral irradiance. *Sol Energy*. 2001;71(5):325-346. doi:[10.1016/S0038-092X\(01\)00054-8](https://doi.org/10.1016/S0038-092X(01)00054-8)
39. Gueymard CA. SMARTS2: a simple model of the atmospheric radiative transfer of sunshine: algorithms and performance assessment, Cocoa, Florida, 1995. [Online]. Available from: <http://instesre.org/GCCE/SMARTS2.pdf>
40. Miller DC. Analysis of transmitted optical spectrum enabling accelerated testing of multijunction concentrating photovoltaic designs. *Optim Eng*. 2011;50(1):013003. doi:[10.1117/1.3530092](https://doi.org/10.1117/1.3530092)
41. Al-Turk S. *Analytic Optimization Modeling of Anti-Reflection Coatings for Solar Cells*. McMaster University; 2011. [Online] <https://macsphere.mcmaster.ca/handle/11375/11272>
42. Birch KP, Downs MJ. Correction to the updated Edlén equation for the refractive index of air. *Metrologia*. 1994;31(4):315-316. doi:[10.1088/0026-1394/31/4/006](https://doi.org/10.1088/0026-1394/31/4/006)
43. Palik ED. *Handbook of Optical Constants of Solids*. London, United Kingdom: Academic Press Limited; 1991. [Online] <https://www.sciencedirect.com/book/9780125444224/handbook-of-optical-constants-of-solids>
44. Jordan DC, Wohlgemuth JH, Kurtz SR. Technology and climate trends in PV module degradation. *27th Eur Photovolt sol Energy Conf Exhib*. 2019;8(1):3118-3124. doi:[10.4229/27thEUPVSEC2012-4DO.5.1](https://doi.org/10.4229/27thEUPVSEC2012-4DO.5.1)
45. Köntges M, Kurtz S, Packard CE, et al. Review of failures of photovoltaic modules. 2014.
46. Jordan DC, Deline C, Johnston S, et al. Silicon heterojunction system field performance. *IEEE J Photovoltaics*. 2018;8(1):177-182. doi:[10.1109/JPHOTOV.2017.2765680](https://doi.org/10.1109/JPHOTOV.2017.2765680)
47. Chen T-C, Yu I-S, Yang Z-P. Hydrogenation behaviors in passivated emitter and rear silicon solar cells with variously hydrogenated  $\text{SiN}_x$  films. *Appl Surf Sci*. 2020;521:146386. doi:[10.1016/j.apsusc.2020.146386](https://doi.org/10.1016/j.apsusc.2020.146386)
48. Miller DC, Bengoechea J, Bokria JG, et al. Examination of an optical transmittance test for photovoltaic encapsulation materials. In Reliability of Photovoltaic Cells, Modules, Components, and Systems VI, Sep. 2013, vol. 8825, p. 882509. doi:[10.1117/12.2024372](https://doi.org/10.1117/12.2024372)
49. Manzoor S, Bertoni M. Degradation of surface recombination velocity at a-Si/c-Si interface under light and temperature. In Conference Record of the IEEE Photovoltaic Specialists Conference, 2021, pp. 1286-1288. doi:[10.1109/PVSC43889.2021.9518982](https://doi.org/10.1109/PVSC43889.2021.9518982)
50. Cho Y-S, Hsu C-H, Lien S-Y, Wu D-S, Hsieh I-C. Effect of hydrogen content in intrinsic a-Si:H on performances of heterojunction solar cells. *Int J Photoenergy*. 2013;2013:1-6. doi:[10.1155/2013/121875](https://doi.org/10.1155/2013/121875)
51. Zhang C, Shen H, Sun L, Yang J, Wu S, Lu Z. Bifacial p-type PERC solar cell with efficiency over 22% using laser doped selective emitter. *Energies*. 2020;13(6):1388. doi:[10.3390/en13061388](https://doi.org/10.3390/en13061388)
52. Duttagupta S, Ma F, Hoex B, Mueller T. Optimised antireflection coatings using silicon nitride on textured silicon surfaces based on measurements and multidimensional modelling. *Energy Procedia*. 2012;15(2011):78-83. doi:[10.1016/j.egypro.2012.02.009](https://doi.org/10.1016/j.egypro.2012.02.009)
53. Witteck R, Veith-Wolf B, Schulte-Huxel H, et al. UV-induced degradation of PERC solar modules with UV-transparent encapsulation materials. *Prog Photovoltaics Res Appl*. 2017;25(6):409-416. doi:[10.1002/pip.2861](https://doi.org/10.1002/pip.2861)
54. Kim BH, Kim G, Park K, Shin M, Chung YC, Lee KR. Effects of suboxide layers on the electronic properties of  $\text{Si}(100)/\text{SiO}_2$  interfaces: atomistic multi-scale approach. *J Appl Phys*. 2013;113(7):073705. doi:[10.1063/1.4791706](https://doi.org/10.1063/1.4791706)
55. Black LE, McIntosh KR. Defect generation at charge-passivated  $\text{Si-SiO}_2$  interfaces by ultraviolet light. *IEEE Trans Electron Devices*. 2010;57(8):1996-2004. doi:[10.1109/TED.2010.2051199](https://doi.org/10.1109/TED.2010.2051199)

56. Schmidt J, Kerr M. Surface passivation of silicon solar cells using plasma-enhanced chemical-vapour-deposited SiN films and thin thermal SiO<sub>2</sub>/plasma SiN stacks. *Semicond Sci Technol*. 2001;16(3): 164-170. doi:[10.1088/0268-1242/16/3/308](https://doi.org/10.1088/0268-1242/16/3/308)
57. Schmidt J, Peibst R, Brendel R. Surface passivation of crystalline silicon solar cells: present and future. *Sol Energy Mater sol Cells*. 2018; 187(September):39-54. doi:[10.1016/j.solmat.2018.06.047](https://doi.org/10.1016/j.solmat.2018.06.047)
58. Bonilla RS, Hoex B, Hamer P, Wilshaw PR. Dielectric surface passivation for silicon solar cells: a review. *Phys Status Solidi*. 2017;214(7): 1700293. doi:[10.1002/pssa.201700293](https://doi.org/10.1002/pssa.201700293)
59. Beckman WA, Bugler JW, Cooper PI, et al. Units and symbols in solar energy. *Sol Energy*. 1978;21(1):65-68. doi:[10.1016/0038-092X\(78\)90118-4](https://doi.org/10.1016/0038-092X(78)90118-4)
60. Miller DC, Kempe MD, Muller MT, Gray MH, Araki K, Kurtz SR. Durability of polymeric encapsulation materials for a PMMA/glass concentrator photovoltaic system. In 10th International Conference on Concentrator Photovoltaic Systems, 2014, pp. 1-35.
61. Miller DC, Bokria JG, Burns DM, et al. Degradation in photovoltaic encapsulant transmittance: results of the first PVQAT TG5 artificial weathering study. *Prog Photovoltaics Res Appl*. 2019;27(5):391-409. doi:[10.1002/pip.3103](https://doi.org/10.1002/pip.3103)
62. Klemchuk P, Ezrin M, Lavigne G, Holley W, Galica J, Agro S. Investigation of the degradation and stabilization of EVA-based encapsulant in field-aged solar energy modules. *Polym Degrad Stab*. 1997;55(3): 347-365. doi:[10.1016/S0141-3910\(96\)00162-0](https://doi.org/10.1016/S0141-3910(96)00162-0)
63. Kempe MD, Moricone T, Kilkenney M. Effects of cerium removal from glass on photovoltaic module performance and stability. In Proceedings of SPIE, Aug. 2009, p. 74120Q. doi:[10.1117/12.825699](https://doi.org/10.1117/12.825699)
64. Borra C, Vlught T, Yang Y, Offerman S. Recovery of cerium from glass polishing waste: a critical review. *Metals (Basel)*. 2018;8(10):801. doi:[10.3390/met8100801](https://doi.org/10.3390/met8100801)
65. King DE, Pern FJ, Pitts JR, Bingham CE, Czanderna AW. Optical changes in cerium-containing glass as a result of accelerated exposure testing [of PV modules]. In Conference Record of the Twenty Sixth IEEE Photovoltaic Specialists Conference - 1997, 1997, pp. 1117-1120. doi:[10.1109/PVSC.1997.654284](https://doi.org/10.1109/PVSC.1997.654284)
66. Long BT, Peters LJ, Schreiber HD. Solarization of soda-lime-silicate glass containing manganese. *J Non Cryst Solids*. 1998;239(1-3): 126-130. doi:[10.1016/S0022-3093\(98\)00728-5](https://doi.org/10.1016/S0022-3093(98)00728-5)
67. Newkirk JM, Nayshevsky I, Sinha A, et al. Artificial linear brush abrasion of coatings for photovoltaic module. *Sol Energy Mater Sol Cells*. 2021;219:110757. doi:[10.1016/j.solmat.2020.110757](https://doi.org/10.1016/j.solmat.2020.110757)
68. Hoex B, Gielis JJH, van de Sanden MCM, Kessels WMM. On the c-Si surface passivation mechanism by the negative-charge-dielectric Al<sub>2</sub>O<sub>3</sub>. *J Appl Phys*. 2008;104(11):113703. doi:[10.1063/1.3021091](https://doi.org/10.1063/1.3021091)
69. Veith-Wolf B, Witteck R, Morlier A, Schulte-Huxel H, Schmidt J. Effect of UV illumination on the passivation quality of AlOx/c-Si interfaces. In 2016 IEEE 43rd Photovoltaic Specialists Conference (PVSC), 2016, pp. 1173-1178. doi:[10.1109/PVSC.2016.7749799](https://doi.org/10.1109/PVSC.2016.7749799)

## SUPPORTING INFORMATION

Additional supporting information can be found online in the Supporting Information section at the end of this article.

**How to cite this article:** Sinha A, Qian J, Moffitt SL, et al.

UV-induced degradation of high-efficiency silicon PV modules with different cell architectures. *Prog Photovolt Res Appl*. 2023; 31(1):36-51. doi:[10.1002/pip.3606](https://doi.org/10.1002/pip.3606)



# UV-induced degradation of high-efficiency silicon PV modules with different cell architectures

Archana Sinha,<sup>1</sup> Jiadong Qian,<sup>2</sup> Stephanie L. Moffitt,<sup>1</sup> Katherine Hurst,<sup>2</sup> Kent Terwilliger,<sup>2</sup> David C. Miller,<sup>2</sup> Laura T. Schelhas,<sup>2\*</sup> Peter Hacke<sup>2+</sup>

<sup>1</sup>SLAC National Accelerator Laboratory, Menlo Park, California, USA

<sup>2</sup>National Renewable Energy Laboratory, Golden, Colorado, USA

## Supplementary Information

### Section SI.1. Test sample preparation

Test samples were prepared by dicing full-size industry-manufactured solar cells down to one-third (for IBC) and one-sixth (for remaining cells) of their original sizes using an optimized laser scribing setup (FiberMark 30, Epilog Laser Corp.) followed by mechanical bending to break. The laser has a nominally 10- $\mu\text{m}$  diameter spot size and was modulated at 80 kHz and operated at 100% stage translation speed. Suns- $V_{oc}$  measurements (WTC-120, Sinton Instruments, Inc.) were performed on the cut cells to confirm that the laser ablation process did not inadvertently cause shunting. Interconnect tabbing ribbons were then manually soldered on the front and rear contact pads of cut cells, with Sn-Pb solder at a controlled unit operating temperature of  $\sim 360^\circ\text{C}$ . For the  $A_{HJ}$  and  $C_{PERT}$  cells, an electrically conductive adhesive (ECA) paste (561-147-2, Engineered Materials Systems, Inc.) was instead applied and cured at  $120^\circ\text{--}125^\circ\text{C}$  for 10 min to form the chemical and electrical bonds between the busbars and tabbing ribbons.

### Section SI.2. Characterization

#### *I-V* measurements

To examine the change in electrical performance as a function of UV dose, front-side *I-V* characterization was performed on the cells in their carrier using a 5600 solar simulator (Eternal Sun Spire) at the cumulative intervals of 0 h, 4 h, 12 h, 24 h, 125 h, 250 h, 500 h, 1000 h, and 2000 h. The 0 h readpoint refers to the measurement done immediately after outdoor light soaking. *I-V* curves were recorded at standard test conditions ( $1000\text{ W/m}^2$  AM1.5G,  $25^\circ\text{C}$ ). In the case of bifacial cells, rear-side *I-V* measurements were also taken if the cell was irradiated through the experiment on the rear side. Additionally, two control cells (stored in the dark) were used for baseline measurements to identify any variation associated with drift in the lamp source and optical system between measurements at each readpoint. No measurable drift was observed through the experiment.

#### Spectral reflectance measurements

For the optical characterization of the cells and packaging materials (representing a PV module), spectral reflectance and transmittance measurements were conducted using an Agilent Cary 7000i two-channel UV-VIS-NIR spectrophotometer equipped with an Agilent DRA-2500 integrating sphere. The position of the mirror was aligned so that the light beam would pass

through the middle of the slit window. Measurements were obtained in 1-nm increments from 200 nm to 2500 nm (for transmittance) and 250 nm to 2500 nm (for reflectance). The baseline correction measurements were performed with a light trap and NIST-certified white Spectralon references that allow for 0% and 100% reflectance. A silica glass control was used as a working reference to identify and correct instrument drift at all readpoints.

### **Secondary ion mass spectroscopy (SIMS)**

The chemical distribution of hydrogen and other elements in the selected samples was measured by secondary ion mass spectroscopy (SIMS) at EAG Laboratories in New Jersey, USA. A pulsed beam of primary ions was focused onto a sample surface, producing secondary ions in a sputtering process. These secondary ions were analyzed to provide information about the elemental species present on the surface. To increase the detection sensitivity at the interfaces, the  $\text{Si}_x\text{N}_y$  was chemically etched to remove the film in  $\text{H}_3\text{PO}_4$  at about  $115^\circ\text{C}$ , assuming an etch rate of  $10 \text{ \AA}/\text{min}$ , and SIMS depth profiling was performed on the underlying interface and Si bulk. For the SIMS depth profiles, the mounting position of test samples was aligned along the cell gridlines (sputter craters were smaller than the distance between gridlines) to keep the crystal orientation the same as the direction of the incident beam. The raw SIMS profiles were given as the secondary ion intensity versus sputter time, which are related to elemental concentration and depth, respectively. In all cases, the H concentration was quantified with respect to Si, as the Si matrix signal was consistent for all samples.

### **X-ray photoelectron spectroscopy (XPS)**

The surface and interface chemistry of select cells were measured by XPS. This analysis was done on the most degraded cell types identified after the UV exposure test. The XPS spectra were collected in a PHI VersaProbe III system ( $\phi$  ULVAC-PHI, Inc.) with a hemispherical analyzer. The X-ray beam spot size was 200- $\mu\text{m}$  diameter and was sensitive to surface analysis, with a penetration depth of 3–7 nm. The neutralizer was used to minimize any charging effects on the cell surface. Elemental depth profiling using a 1-keV Ar ion sputtering gun was performed on the cell front non-metalized surfaces. The Ar ion beam was rastered over a small area of  $2 \times 2 \text{ mm}$ , larger than the X-ray beam spot size for data acquisition. The etch rate for the silicon solar cell specimens was estimated relative to standard  $\text{SiO}_2$  reference material. After a brief pre-sputter to remove surface contaminants, the high-resolution XPS spectra at each etch step were collected at pass energy of 55 eV and energy resolution of 0.1 eV. The data were acquired with multiple sweeps to increase the signal-to-noise ratio. The binding energy scale calibration was done using an adventitious carbon (C 1s) peak at 284.8 eV. Overlapping peaks were resolved into individual components by fitting Gaussian-Lorentzian functions, and the atomic composition was obtained from integrated peak intensities using the CasaXPS software package (Casa Software Ltd.).

### **Optical microscopy and RGB colorimetry**

Microscope images were taken on a VHX 5000 Digital Microscope (Keyence Corp.). Cross-polarized images were taken using Keyence VH-Z100 filters at 200x magnification to achieve color saturation and reduce glare using the “Full Coaxial” (bright field) illumination at maximum intensity. Before taking images, the microscope was white balanced using the white standard provided with the microscope. High-resolution high dynamic range (HR-HDR, 1.92 Mpix) images were taken to increase the image contrast for feature identification. To observe the integrity of the metallization and cell surface, images were taken in at least three locations on each sample: the middle (M), lower middle (LM), and lower right (LR). Red, green, and blue values were extracted

in five locations (top, center, bottom, left, and right) on each image to quantify the color of the cell surface using the eyedropper tool in Photoshop software (Adobe, Inc.)

### Supporting Figures and Tables

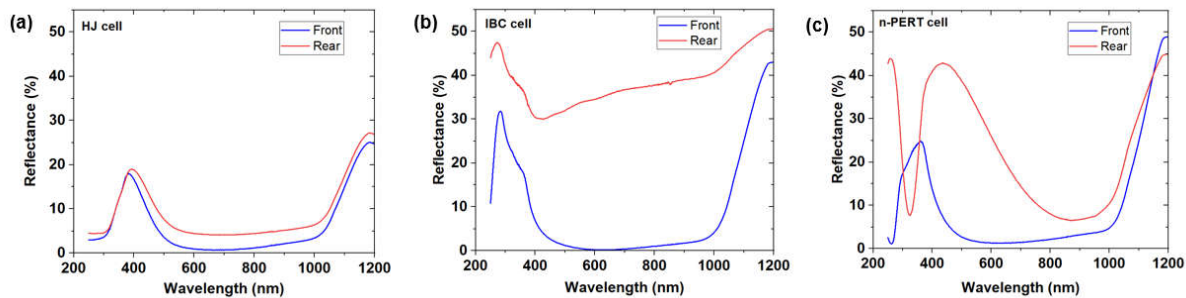


**FIGURE SI.1** Measured hemispherical reflectance of the three cell types in the unaged condition (a)  $A_{HJ}$ , (b)  $B_{IBC}$ , and (c)  $D_{PERT}$ . In addition to the IBC cell, differences in the reflectance of the HJ and n-PERT cells may result from some differences in metal gridline geometry and layers stacked at the front and rear surfaces.

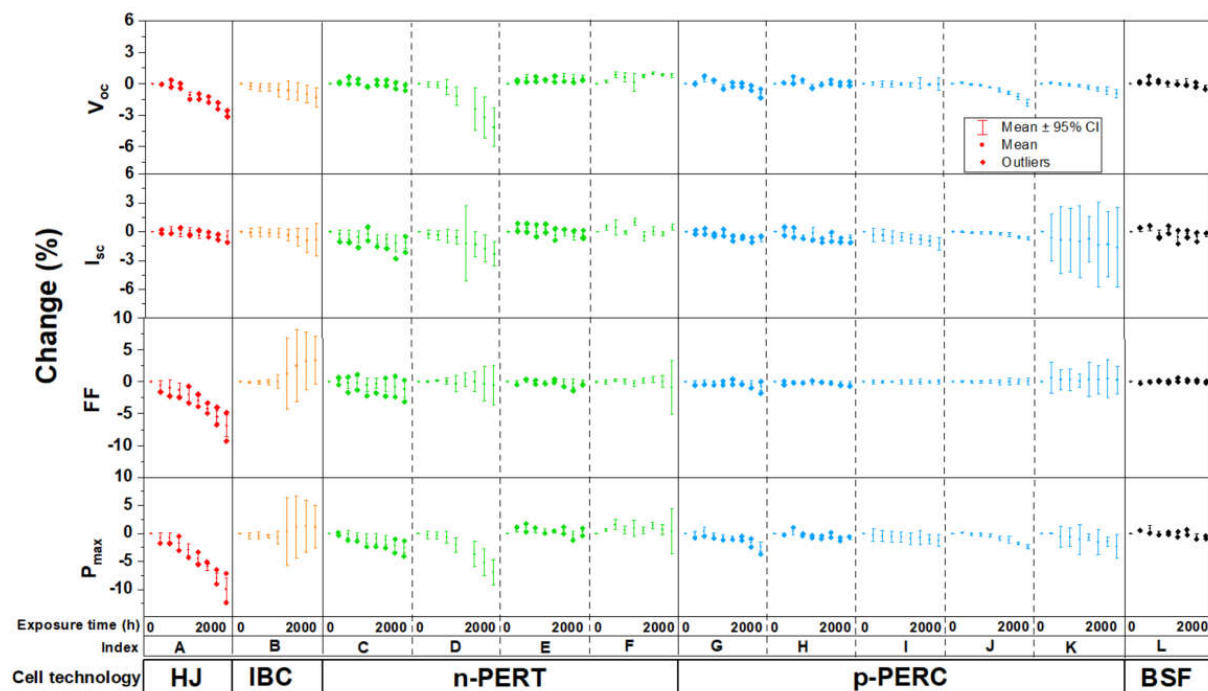


**FIGURE SI.2.** The degradation in  $I$ - $V$  parameters measured at both labs for all replicates of each cell type along with a 95% confidence interval in the measurement at each readpoint.

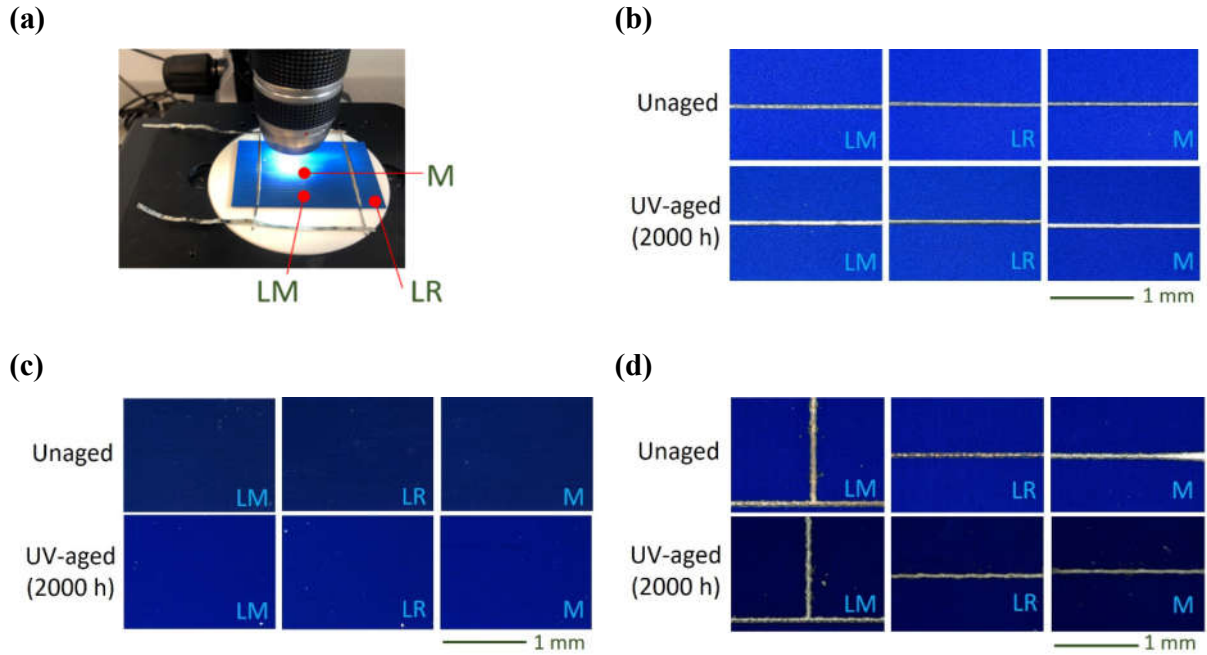


**FIGURE SI.3.** (a) Optical microscopy setup with a test cell, indicating three regions of interest on the front surface where images are collected for cells (b) A<sub>HJ</sub>, (c) B<sub>IBC</sub>, and (d) D<sub>PERT</sub>. Distinctive changes in the blue color of Si<sub>x</sub>N<sub>y</sub> coating for cells (c) and (d) are visible, which is also consistent with the changes in their respective reflectance spectra at shorter wavelengths 250-450 nm. IBC cell (c) became lighter blue, while n-PERT cell (d) turned darker blue after 2000 h of UV exposure. The factor(s) motivating the change in color was not examined but may include changes in thickness, composition, or density. No obvious differences in the gridline color or morphology were detected after UV exposure.

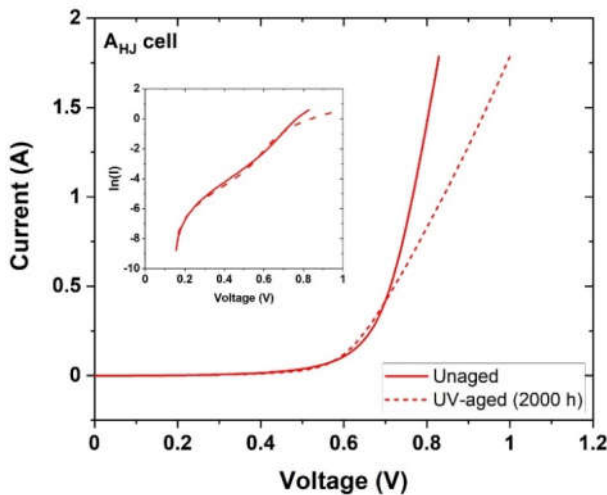


**FIGURE SI.4.** Dark *I-V* curves for the bifacial A<sub>HJ</sub> cell before (solid) and after (dashed) 2000 h of UV exposure testing. Inset shows the y-axis (current) in a logarithmic scale, indicating



an increase in diode ideality factor and recombination current in the cell after UV exposure. An increase in  $R_s$  is also observed by the change in the slope at a higher voltage closer to  $V_{oc}$ .

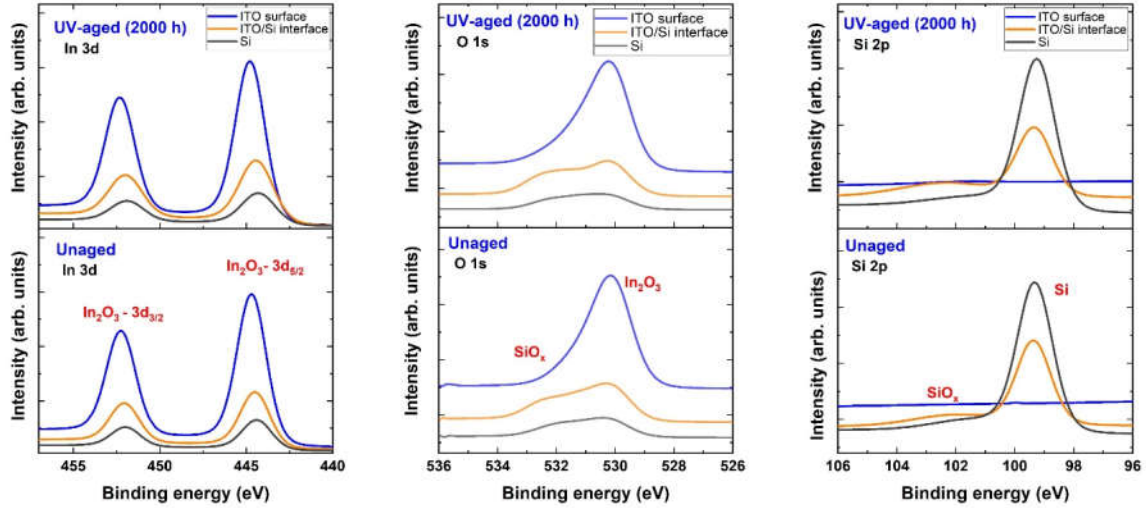


**FIGURE SI.5.** High-resolution XPS spectra obtained on the front surfaces of unaged and UV-aged (for 2000 h)  $A_{HJ}$  samples for In 3d, O 1s, and Si 2p. Elemental depth profiles shown here are at three regions: the  $Si_xN_y$  surface,  $SiO_x/Si$  interface, and Si bulk. The In 3d spectrum contains two distinct symmetric peaks separated by 7.6 eV, which correspond to  $In_2O_3$ . The peak intensity decreases with increasing depth; however, no spectral shifts are observed in either unaged or aged samples. The O 1s peak changes its shape with depth; a shoulder emerges at higher binding energy ( $\sim 532$  eV). The intense peak at 530.6 eV is assigned to the oxygen bound to indium and tin in the ITO layer, while the broad shoulder at  $\sim 532$  eV arises from an ultra-thin  $SiO_x$  layer at the ITO/Si interface [1]. The Si 2p peak is absent at the front surface and only emerges when it reaches the a-Si layer. However, no significant differences between the two samples are observed, suggesting no measurable change in the  $SiO_x$  layer thickness. Overall, the elemental peak shapes or positions of the aged sample are similar to the unaged sample, suggesting that there are no major changes to the chemistry or bond configuration at the cell interfaces beyond the hydrogen measured by SIMS.

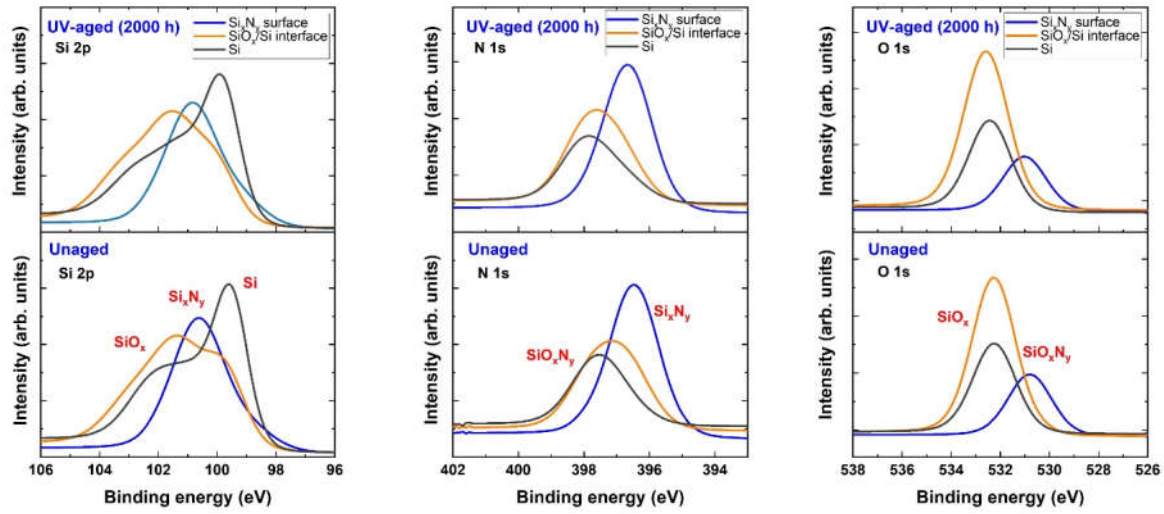


**FIGURE SI.6.** High-resolution XPS spectra obtained on the front surfaces of unaged and UV-aged (for 2000 h) BIBC samples for Si 2p, N 1s, and O 1s. Elemental depth profiles shown here are at three regions: the  $\text{Si}_x\text{N}_y$  surface,  $\text{SiO}_x/\text{Si}$  interface, and Si bulk. The N 1s peak on the surface is assigned to  $\text{Si}_x\text{N}_y$  (396.4 eV) [2], which is shifting toward higher binding energy as we move down into the silicon. The Si 2p peak at the surface can be fitted with two components, the central peak at 100.9 eV, corresponding to  $\text{Si}_x\text{N}_y$ , and an adjacent peak, which can be assigned to silicon oxynitride ( $\text{SiO}_x\text{N}_y$ ) and/or  $\text{SiO}_x$ . Drastic chemical shifts are observed at the  $\text{Si}_x\text{N}_y/\text{Si}$  interface, where  $\text{Si}_x\text{N}_y$  diminishes and two new peaks emerge at 99.6 eV and 102 eV, assigned to elemental silicon and oxide, respectively. The O 1s peak on the surface is designated to  $\text{SiO}_x\text{N}_y$  (531 eV) [2], which almost disappears at  $\text{Si}_x\text{N}_y/\text{Si}$  interface, and a new peak at higher binding energy ( $\text{SiO}_x$ , 532.3 eV) appears. The BIBC cell also did not show any significant chemical changes after UV irradiation.

## REFERENCES

- [1] S. Sheng et al., “XPS depth profiling study of n/TCO interfaces for p-i-n amorphous silicon solar cells,” *Appl. Surf. Sci.*, vol. 253, no. 3, pp. 1677–1682, 2006.
- [2] P. Singh, S. M. Shivaprasad, M. Lal, and M. Husain, “Angle-dependent XPS analysis of silicon nitride film deposited on screen-printed crystalline silicon solar cell,” *Sol. Energy Mater. Sol. Cells*, vol. 93, no. 1, pp. 19–24, 2009.